Main Manuscript for

MRP5 and MRP9 Play a Concerted Role in Male Reproduction and Mitochondrial Function

Ian Chambers[1], Praveen Kumar[2], Jens Lichtenberg[3], Pengcheng Wang[2], Jianshi Yu[2], John Phillips[4], Maureen Kane[2], David Bodine[3], Iqbal Hamza[1]

[1]Department of Animal & Avian Sciences and Department of Cell Biology & Molecular Genetics, University of Maryland, College Park, MD, USA

[2]Department of Pharmaceutical Sciences, University of Maryland School of Pharmacy, Baltimore, MD, USA

[3]Genetics and Molecular Biology Branch, National Human Genome Research Institute, National Institutes of Health, Bethesda, MD, USA

[4]Department of Medicine, University of Utah School of Medicine, Salt Lake City, UT, USA

Corresponding Author: Iqbal Hamza

Email: hamza@umd.edu

Author Contributions:

IGC: Conceptualization, Methodology, Investigation, Formal analysis, Validation, Visualization, Writing—original draft, Writing—review and editing

PK: Conceptualization, Methodology, Investigation, Formal analysis, Validation

JL: Methodology, Investigation, Formal analysis, Validation, Visualization

PW: Methodology, Investigation, Formal analysis

JY: Methodology, Investigation, Formal analysis

JP: Conceptualization, Methodology, Investigation, Formal analysis, Validation, Resources, Funding acquisition, Writing—review and editing

MAK: Conceptualization, Methodology, Investigation, Formal analysis, Validation, Resources, Funding acquisition, Writing—review and editing

DB: Conceptualization, Methodology, Investigation, Formal analysis, Validation, Resources, Funding acquisition, Writing—review and editing

IH: Conceptualization, Methodology, Investigation, Formal analysis, Validation, Visualization, Resources, Software, Supervision, Funding acquisition, Writing—original draft, Writing—review and editing

Competing Interest Statement:

IH is the President and Founder of Rakta Therapeutics Inc. (College Park, MD), a company involved in the development of heme transporter-related diagnostics. He declares no other competing financial interests.

Classification: Biological Sciences, Genetics

Keywords: Multidrug Resistance Proteins (MRPs), Reproduction, Heme, Mitochondria Associated Membranes (MAMs), Fertility

This PDF file includes:

Main Text
Figures 1 *to* 6

Abstract

Multidrug Resistance Proteins (MRPs) are transporters that play critical roles in cancer even though the physiological substrates of these enigmatic transporters are poorly elucidated. In *Caenorhabditis elegans*, MRP5/ABCC5 is an essential heme exporter as *mrp-5* mutants are unviable due to their inability to export heme from the intestine to extra-intestinal tissues. Heme supplementation restores viability of these mutants but fails to restore male reproductive deficits. Correspondingly, cell biological studies show that MRP5 regulates heme levels in the mammalian secretory pathway even though MRP5 knockout (KO) mice do not show reproductive phenotypes. The closest homolog of MRP5 is MRP9/ABCC12, which is absent in *C. elegans* raising the possibility that MRP9 may genetically compensate for MRP5. Here, we show that MRP5 and MRP9 double KO mice are viable but reveal significant male reproductive deficits. Although MRP9 is highly expressed in sperm, MRP9 KO mice show reproductive phenotypes only when MRP5 is absent. Both ABCC transporters localize to mitochondrial-associated membranes (MAMs), dynamic scaffolds that associate the mitochondria and endoplasmic reticulum. Consequently, DKO mice reveal abnormal sperm mitochondria with reduced mitochondrial membrane potential and fertilization rates. Metabolomics show striking differences in metabolite profiles in the DKO testes and RNA-seq show significant alterations in genes related to mitochondrial function and retinoic acid metabolism. Targeted functional metabolomics reveal lower retinoic acid levels in the DKO testes and higher levels of triglycerides in the mitochondria. These findings establish a model in which MRP5 and MRP9 play a concerted role in regulating male reproductive functions and mitochondrial sufficiency.

Significance Statement

MRPs are typically implicated in cancer biology. Here, we show that MRP9 and MRP5 localize to mitochondrial-associated membranes and play a concerted role in maintaining mitochondrial homeostasis and male reproductive fitness. Our work fills in significant gaps in our understanding of MRP9 and MRR5 with wider implications in male fertility. It is plausible that variants in these transporters are associated with male reproductive dysfunction.

Main Text

Introduction

Multidrug Resistance-associated Proteins (MRPs) belong to the type C subclass of the ATP Binding Cassette (ABCC) transporters, a highly conserved family of proteins that have been studied for decades for their role in cancers (1-7). MRPs are notoriously upregulated in a number of malignancies because of their ability to efflux a wide range of synthetic and chemotherapeutic agents, conferring cancer cells resistance to drug treatments (3, 8-11). Due to their critical importance in human health and clinical outcomes, myriads of MRP substrates have now been identified, particularly from *in vitro* studies of tumor cell lines (3, 4, 6, 12, 13). However, the promiscuity of drugs effluxed in this context is likely a functional consequence of cancer cells hijacking these active transporters rather than that being their true evolutionary role. Therefore, a major outstanding item remaining in the MRP field is the determination of true physiological functions and substrates for a number of these transporters.

Previous work from our group shed some light on the function of one such ABCC transporter, MRP5/ABCC5, where studies in worms, yeast, zebrafish and mammalian cells demonstrated it to be a heme exporter (14). Prior to this discovery, the role of MRP5 appeared to be that of cyclic nucleotide export from cells as demonstrated by transport of cGMP in membrane vesicles expressing human MRP5 *in vitro* (12, 15). However, the generation of MRP5 null mice demonstrated little to no contribution in cGMP efflux and no observable overt phenotypes, leaving the physiological relevance of this transporter unclear outside its *in vitro* or cancer cell context (16, 17). This is not the case in *C. elegans*, a heme auxotroph, where MRP-5 is absolutely essential for intercellular heme trafficking and knockout of *mrp*-5 results in heme deficiency and embryonic lethality (14).

While cell biological studies in mouse embryonic fibroblasts from MRP5 KO mice confirmed that MRP5 indeed plays a conserved role in heme export i.e. transporting heme into the secretory pathway for incorporation into hemoproteins or exporting it from the cell across the plasma membrane (14, 18-20), MRP5 KO mice do not show any heme-related phenotypes *in vivo*. A postulated hypothesis to explain these differences could be genetic compensation by other closely related transporters, which are phylogenetically conserved in higher order eukaryotes but absent in the *C. elegans* genome (14, 21). A candidate for this proposed compensation and further functional delineation is MRP9/ABCC12, the closest relative of MRP5 and one of the last of the ABCC proteins to have been discovered (6, 22, 23). MRP9 is highly expressed in male reproductive tissues but fails to effectively efflux drugs *in vitro*, and its endogenous function remains to be elucidated (6, 24, 25).

In this work, we generate a MRP9 knockout and MRP9 / MRP5 double knockout (DKO) mouse models to fully characterize these transporters' physiological functions. Loss of MRP9 and MRP5 disrupts mitochondrial homeostasis and regulatory pathways in the testes, with RNA-seq and metabolomic analyses revealing large-scale perturbation in genes and metabolism related to mitochondrial function. Together, these results establish a concerted and critical role for MRP9 and MRP5 in male reproduction and mitochondrial metabolism, implying that the ancestral role of MRP5 in *C. elegans* reproduction was co-opted in the vertebrate ancestor.

Results

Loss of MRP9 in mice induces the expression of MRP5 in the testes

C. elegans mrp-5(ok2067) deletion mutants are lethal unless rescued with dietary heme supplementation (14). Serendipitously, we found that even in the presence of heme *mrp-5(ok2067)* male worms are defective in mating **(Figures S1A and S1B)**. These worms exhibit defective mating apparatus with stunted tail fan formation, reduced numbers of rays, and spicules which fail to retract despite normal mating behaviors. Given that hermaphrodite *mrp-5* knockout worms mate normally with wildtype males (not shown), it would appear the defect is paternal. For these reasons, we hypothesized that MRP-5 may have additional functions related to male

128 reproduction outside of its traditional role in heme transport and homeostasis. MRP5 knockout
129 mice however show no reproductive deficiencies, prompting inquiry into other ABCC transporters
130 that may genetically compensate for the loss of MRP5 in higher order vertebrates.
131 Phylogenetic analysis of ABCC transporters across metazoans confirmed that members
132 of the short MRP clade (ABCCs - 4, 5, 7, 11, 12) cluster tightly together across species indicating
133 their evolutionary relation (6, 14). Within this subclade, *C. elegans* has only MRP-5 whereas most
134 vertebrates have an additional paralog, MRP9 **(Figure 1A)**, which is conserved in all higher-order
135 vertebrates but remains to be fully characterized *in vivo.* We therefore generated MRP9 mutant
136 mice via CRISPR/Cas9 to explore MRP9's endogenous functions. Utilizing guide RNAs targeted
137 to the second exon of *Abcc12* we were able to generate 11 founder animals with various indels at
138 the target site and a 17 bp insertion line was selected for further characterization **(Figures 1B**
139 **and S1C)**. RT-PCR confirmed that the frameshift-inducing mutation was transcribed with no
140 alternate start sites or splice variants identified **(Figure S1D)**.
141 *Abcc12-/-* animals are viable and reach adulthood with no overt phenotypes.
142 Immunoblots of lysates from testes of adult mice confirmed no detectable MRP9 protein in
143 knockout animals **(Figure 1C)**. Immunohistochemistry of tissue sections showed MRP9 in both
144 the maturing and developed spermatozoa of seminiferous tubules and caudal epididymis,
145 respectively, consistent with the findings reported by Ono et al **(Figure 1D)** (24). Recent single
146 cell RNAseq datasets of the testis niche further confirmed these findings as the gene expression
147 profile of *Abcc12* is distinctly germ cell specific **(Figure S1E)** (26). This is in contrast to *Abcc5*,
148 which appears to be normally expressed in early spermatogonia precursors as well as Sertoli and
149 Leydig cells **(Figure S1E)**. Immunoblotting of lysates from additional tissues of wildtype and KO
150 mice revealed the testes as the only organ with any appreciable amounts of both, MRP9 and
151 MRP5 **(Figure 1C)**. Importantly, MRP9 KO testes showed elevated levels of MRP5 raising the
152 notion that MRP5 could be compensating for MRP9 deficiency in the testes **(Figures 1E and 1F)**.

153 **MRP9 and MRP5 are required for male reproductive fitness**

154 MRP9 KO mice do not show any statistically significant defects in reproduction, with
155 expected litter sizes and normal Mendelian F1 segregation when intercrossed [n = 166, Chi-
156 squared = 0.976, *P* value = 0.614] **(Figure 2A)**. MRP9 KO crossed to MRP5 KO mice
157 successfully generated DKO mice which reached adulthood with no overt phenotypes. Although
158 DKO mice were viable, they were deficient in their reproductive capacity; the average number of
159 pups from intercrosses of DKO mice were significantly reduced compared to WT [n > 33 litters, *P*
160 value < 0.0001] **(Figure 2B)**. Interestingly, fecundity was restored back to single KO levels when
161 DKO females were crossed with WT or double heterozygous males alone, suggestive that the
162 failure may be paternal [n > 21 litters, *P* value < 0.0001] **(Figure 2B)**. Furthermore, DKO male
163 mice setup to breed had high incidences of penile prolapse and clogging of their urogenital tracks
164 with seminal coagulum (five DKOs compared to zero WT male mice), regardless of the female
165 genotype **(Figure 2C)**. These findings, taken together with our protein expression data, prompted
166 a closer investigation into male fitness as the major defect behind the DKO reproductive failure.
167 Indeed, sperm from DKO mice had significantly lower *in vitro* fertilization (IVF) rates compared to
168 wildtype **(Figure 2D)**. Interestingly this may be attributed to sperm fitness / quality rather than
169 quantity as DKO sperm showed trends of decreased motility with no differences in total sperm
170 production **(Figures S2A, S2B and 2E)**.

171 **MRP9 is localized to mitochondrial associated membranes in the testes**

172 To understand why DKO male mice have reduced fecundity and sperm fitness we further
173 characterized the function of these proteins in this context. Given their distinct spatiotemporal
174 gene expressions **(Figure S1E)**, we hypothesized that these MRPs may play overlapping
175 subcellular roles during spermatid maturation. The Borst group had shown that MRP9 is localized
176 to the sperm midpiece (24, 27, 28), and when expressed in HEK293 closely resembled an ER
177 localization (24). In polarized MDCKII cells, transfection of *ABCC12* showed a distinct intracellular
178 distribution of MRP9 in stark contrast to MRP5 that localized primarily to the basolateral surface

179 of the plasma membrane **(Figure 3A)**. To determine if this was also the case *in vivo* or merely a
180 consequence of ectopic expression, we performed subcellular fractionation of lysates from mouse
181 testes. Immunoblotting showed that MRP9 protein was actually significantly enriched in 9,000 *x g*
182 fractions which pellet mitochondria **(Figure 3B)**. This result was surprising given previously
183 published findings (24, 29, 30), and that MRP9 lacks any obvious mitochondrial targeting
184 sequences. However, an explanation for this unexpected result could be that mitochondrial-
185 associated membranes (MAMs), the contact sites of the ER which are intimately associated with
186 the mitochondria, are enriched in our crude mitochondrial fractions (31-34).
187 Next, we performed Airyscan super resolution microscopy on HeLa cells transiently
188 transfected with human *ABCC12* **(Figure 3C)**. 3D rendering revealed that MRP9 was in close
189 proximity or at the interface of the mitochondria (Mitotracker) and ER (Calnexin) **(Figure 3C and**
190 **Movie S1)**. To validate this localization, we performed Percoll-based differential centrifugations to
191 further separate crude mitochondrial fractions into purified mitochondria and MAMs from testes
192 tissue homogenates (32). Immunoblots of distinct testes fractions revealed that MRP9 was in fact
193 not present in purified mitochondria but significantly enriched in MAMs, characterized by the
194 markers Mitofusin 2 and Calnexin **(Figure 3D)**. Interestingly, probing for MRP5 from these same
195 fractions indicated that it too was enriched in the MAMs as well as total membranes **(Figure 3E)**.
196 These results indicate that subcellular expression patterns of MRPs may vary dependent on
197 tissue contexts.

198 **Multi-omics of DKO testes reveals extensive perturbation and mitochondrial dysfunction**

199 In order to systematically dissect why the combined loss of MRP9 and MRP5 manifests
200 in male reproductive dysfunction, we sought to understand what substrates may be transported
201 by these proteins and how their absence may impact homeostatic pathways in the testes. To
202 achieve this, we performed untargeted metabolomics and RNAseq from paired testes of the same
203 mice to integrate any differential metabolites and gene expression changes **(Figure S3A)**. Global
204 untargeted metabolomics of testes indicated significant perturbation, with 24 of the top 25
205 differential species measured from negative ion mode acquisition of aqueous phase metabolites
206 showing accumulation in the DKO **(Figure 4A)**. Dramatic differences in metabolite profiles were
207 evident however regardless of the extraction method (aqueous vs organic) or the ion mode of
208 acquisition (negative vs positive) **(Figures S3B and S3C)**. Analysis of these data allowed for the
209 identification of mass-to-charge ratios (m/z) of hyper-accumulated candidate metabolites.
210 However, given our sampling was untargeted, a particular *m/z* could represent multiple
211 possibilities of actual biological compounds even given the high mass accuracy and resolution of
212 the Q-TOF platform. As a means to associate these putative species with specific metabolites, all
213 significant m/z's identified from our six untargeted datasets were pooled and processed using
214 MetaboAnalyst Mummichog analyses (35). From the species of interest analyzed, 65 metabolites
215 were assigned possible KEGG IDs **(Table S1)**. Amongst these, succinyl-CoA, which is also an
216 essential TCA cycle energy source and a heme precursor, had the largest fold-change increase
217 in DKO testes (36, 37).
218 RNAseq analysis from the same tissues found 3,736 differentially expressed genes
219 between WT and DKO, with a number of top genes differentially expressed including
220 uncharacterized and testis-specific predicted genes (*Gm10354*, *Gm9758*, *5430401F13Rik*) as
221 well as mitochondrial respiratory genes (*Atp5k*, *Ndufa1*, *Atp5e*) **(Figure 4B)**. To unbiasedly
222 determine the pathways and Gene Ontology (GO) terms most significantly affected in these mice
223 we performed Ingenuity Pathway Analysis (IPA) **(Figures 4C and S3D)**. The majority of the top
224 GO canonical pathways identified by IPA were intimately interconnected and overlapped with
225 mitochondrial function (**Figures 4C and 4D**). Of note, the top two pathways identified, EIF2
226 Signaling and Protein Ubiquitination, are critical for mitigating unfolded protein response and
227 mitochondrial dysfunction associated with iron and heme deficiencies (38).
228 To generate metabolite-gene relationships, we integrated our metabolomics and RNAseq
229 data using MetaboAnalyst Joint Pathway Analysis. The merged data analysis revealed significant
230 mitochondrial pathway dysfunction with energy production components of the cell (TCA Cycle,

231 Pyruvate Metabolism, and Glycolysis) showing the highest impact **(Figure 4E)**. Taken together,
232 these findings reinforce a role for MRP9 and MRP5 in mitochondrial metabolism in the testes.

233 **EIF2a phosphorylation and associated signaling pathways mitigate mitochondrial**
234 **dysfunction**

235 Having identified mitochondrial dysfunction as the overarching factor from our integrative
236 analysis, we sought to determine the specific mechanisms that underlie this dysfunction in the
237 testes. Mining our RNAseq dataset, we built an analysis pipeline to determine and curate fold
238 changes of all genes associated with a given pathway from published GO databases for
239 downstream investigation and mapping. In querying all genes associated with the mitochondria
240 and mitochondrial dysfunction, we identified over 200 dysregulated genes (**Figure 5A**). We then
241 asked what individual genes or pathways may be involved in responding to such a significant
242 level of disruption. Given the top-related pathway identified from our IPA studies was EIF2
243 signaling, we investigated all associated genes and found 95 that were perturbed in DKO testes
244 (**Figure 5B**). EIF2 signaling and EIF2a phosphorylation by the heme responsive kinase HRI
245 (*Eif2ak1*) are established mechanisms for regulating translation to reduce mitochondrial stress
246 and unfolded protein response (UPR) in situations of intracellular heme deficiency (38-41). In
247 particular this model is well documented in the erythron, where heme is critical as it becomes the
248 limiting factor for incorporation into hemoglobin for red blood cell differentiation **(Figure S4A)**.
249 Limited studies have characterized a similar role in mitigating mitochondrial dysfunction in
250 neurons, but very little is known about HRI and EIF2a signaling in other tissues such as the testes
251 (39, 42-45). Indeed, analysis of the testes single cell RNAseq dataset determined that both
252 factors are expressed during spermatid maturation **(Figure S4B)**, and immunoblotting of total
253 testes homogenates confirmed significant EIF2a protein expression **(Figure 5C)** (26). Importantly,
254 EIF2a phosphorylation was significantly increased in the DKO mice, substantiating the
255 involvement of the EIF2a pathway in mitigating UPR and mitochondrial dysfunction in the testes
256 **(Figure 5C and 5D)**. We next asked if the observed EIF2 signaling in the testes of DKO mice was
257 in response to heme deficiency, as is the hallmark in the erythron. If so, one would expect that
258 iron/heme homeostasis should also be perturbed in the testes of these mice. Subsequent probing
259 with our pipeline pathway revealed heme and iron homeostasis related genes were in fact
260 significantly altered **(Figure S4C)**. To determine if heme levels themselves were also impacted,
261 we measured total heme in male reproductive tissues. Heme levels in the caudal epididymides,
262 the storage sites for mature sperm, showed a significant decrease **(Figure 5E)**, while whole
263 testes and seminal vesicles showed no differences **(Figure S4D and S4E)**. These results
264 suggest that there is insufficient heme specifically in spermatozoa of DKO mice.

265 A critical component of the canonical EIF2 signaling cascade for maintaining
266 mitochondrial function and redox homeostasis is the alteration of mTOR signaling to inhibit
267 proliferation and enable differentiation (38, 46). Indeed, the mTOR signaling pathway was one of
268 the most significant GO terms identified by IPA **(Figure 4C and S3D)**, which we also validated
269 with our analysis pipeline **(Figure S5A)**. Upregulation of EIF-4E, a highly abundant translation
270 regulation factor in the testes, has been shown to play an important role in spermatogenesis
271 through regulation of capping stage-specific mRNAs during germ cell development (47). A
272 modulator of these related pathways is retinoic acid, which has been implicated in mTOR/EIF-4E
273 cascade and plays a key role in a variety of biological contexts including regulation of genes
274 impacting mitochondrial function (48-52). Principal targets of retinoic acid include key OxPhos
275 and respiratory genes such as NADH dehydrogenase subunits, cytochrome c oxidases and the
276 ATPases, some of the top differentially expressed genes from our RNAseq **(Figure 4B)** (51, 53).
277 Investigation of retinoic acid related genes revealed significant perturbation including decreases
278 in the cytosolic chaperone *Crabp1*, responsible for delivering retinoic acid for catabolism, as well
279 as binding receptors (RAR, RXRs), suggestive of dysregulated retinoic acid homeostasis **(Figure**
280 **S5B)** (54-56). Importantly, retinoic acid signaling is essential for male germ cell differentiation,
281 exerting key control over meiotic initiation and spermatogenesis, with defects in retinoid
282 homeostasis a well-established cause of male infertility (57-60). Taken together, we hypothesized
283 that retinoic acid homeostasis/signaling may play an important role in the phenotypes observed in

our DKO mice. Quantification of the major components of the retinoid pathway revealed that total levels of vitamin A (retinol) and storage esters were not perturbed in the testes **(Figure S5C and S5D)**, but all-*trans* retinoic acid levels were significantly reduced DKOs compared to wildtype **(Figure S5E)**. Other retinoic acid isomers were unchanged (13-*cis* retinoic acid, 9,13-di-*cis* retinoic acid) or below the limit of detection (9-*cis* retinoic acid) (data not shown).

To further validate if retinoic acid binding transcription factors and cascade regulators were indeed impacting mitochondrial genes of interest, we performed unbiased motif discovery on regulatory sequences of all up-regulated and down-regulated genes from our pathway pipeline **(Figure 5A and S5F)**. The top five statistically significant DNA sequences identified were further analyzed and queried against known binding motifs. With two independent analysis platforms (MEME suite and HOMER) we identified significant enrichment of conserved retinoic acid related binding motifs including putative RXRs and RORA binding sequences **(Figure S5F)** (61). These findings suggest a mechanistic link between transcripts related to mitochondrial dysfunction, retinoid signaling genes, and decreased retinoic acid levels, corresponding with a specific enrichment of retinoic acid binding motifs in the DKO mice.

Ablation of MRP9 and MRP5 significantly damages sperm mitochondria

To determine whether mitochondrial disruption could be inducing the gene expression and metabolomic changes that in-turn impact sperm fertilization in the DKO testes, we analyzed mitochondria oxidative phosphorylation complexes in total testes lysates. However, all five complexes appeared to be normal and unchanged in DKOs **(Figure S6A)**. We next fractionated the testes and performed high-throughput targeted metabolomics on each isolated fraction, allowing for the identification and quantification of specific metabolites within each subcellular niche **(Figure S6B)**. We found that the mitochondria and MAM fractions of the DKO testes hyper-accumulate triglycerides, indicative of mitochondrial metabolism dysfunction **(Figure S6C and S6D)** (62, 63).

Mature caudal epididymal sperm were then collected from WT and DKO adult mice by swim-out for mitochondrial membrane potential ($\Delta\Psi_M$) analysis and transmission electron microscopy (TEM). Staining of sperm with JC-1 revealed that DKO mice have reduced J aggregates and $\Delta\Psi_M$ compared to WT **(Figure 7A, 7B and S7A)**. Strikingly, TEM cross sections of sperm midpieces revealed DKO mice also have highly vacuolated and aberrant mitochondria, in contrast to the ubiquitously electron dense cristae in the WT **(Figure 7C)**. These defects were not observed in the single KOs or double heterozygous animals **(Figure S7B)**.

Discussion

ABCC proteins are one of the most well-studied class of transporters due to their critical roles in cancer biology, multidrug resistance and associated human diseases (3, 64-67). Taken together, our studies fill significant gaps in our understanding of not only of MRP9 but also MRP5, uncovering novel endogenous functions related to reproduction. Given MRP5 is genetically dispensable in the mouse model with low gene expression in male reproductive tissues, no studies have examined its protein levels or function in the testes (14, 68-70). Klein et al showed a weak MRP5 signal in Leydig cells of rats but nothing in macaque or human testis (71). We show that MRP5 is detectable in the testes, but that it also appears to be enriched in mitochondrial associated membranes along with MRP9. Though MRP5 still localizes to basolateral plasma membranes in polarized MDCKII cells, our tissue fractionation studies bring to light the possibility of additional novel tissue dependent expression patterns and subcellular localizations for this well studied transporter. We envision that these results may have significant implications when it comes to cancer and the distinct roles MRPs may play dependent upon tissue / cell type. We propose the following model for the concerted function of MRP9 and MRP5 in the testes **(Figure 7D)**: In the absence of MRP9 and MRP5, metabolites such as heme and/or other substrates, are inappropriately trafficked or distributed causing mitochondrial damage. This dysfunction induces signaling through the EIF2 and mTOR pathways to regulate protein translation and UPR with corresponding changes in retinoic acid levels and signaling. Germ cells differentiate into mature

335 spermatozoa, but these are functionally defective as they fail to fertilize normal oocytes due to
336 mitochondrial insufficiencies.
337 MRP9 is an enigmatic ABCC transporter. It has a unique expression pattern, no known
338 drug substrates, and the last in the ABCC class still to be characterized (6, 24, 25). In the current
339 study, we fill in some of the gaps in our knowledge by generating an MRP9 knockout mouse
340 model to explore its endogenous functions. We find that MRP9 is specifically expressed in
341 developing spermatids and mature spermatozoa in mice and unlike most other MRPs, MRP9
342 does not localize to the plasma membrane irrespective of cell polarization, consistent with the
343 published findings of Ono et al (24). Contrary to other reported studies however, MRP9 is not
344 endogenously expressed in any cell lines tested in our hands, including primary mouse
345 embryonic fibroblasts, and MRP9 protein cannot be induced by sodium butyrate treatment
346 **(Figure S8)** as was reported recently (72).
347 Transient transfections and tissue fractionations provide strong evidence that MRP9
348 partitions specifically to mitochondrial-associated membranes of the testes, a distinct
349 compartment characterized by mitochondrial outer membrane and endoplasmic reticulum
350 markers. This is physiologically reasonable as MRP9 is localized to developing and mature
351 spermatozoa which are known to be devoid of traditional ER structures (73, 74). Though the ER
352 is depleted in the process of differentiation, vestiges of ER membranes likely remain, particularly
353 those in tight contact with mitochondria, and have been postulated to concentrate in the neck of
354 the sperm midpiece to serve as a store for Ca^{2+} necessary for sperm activation (74, 75). Indeed,
355 ER resident proteins such as ERp29 and Calreticulin have also been demonstrated to be present
356 in sperm and play essential roles in acrosome reaction, fertilization and stress responses (74,
357 75). We envision MRP9 may reside at these interfaces adjacent to mitochondria of the midpiece,
358 effluxing substrates essential for regulating mitochondrial function and/or trafficking metabolites
359 between these compartments as spermatogonia develop.
360 Loss of MRP9 alone has no discernable impact on male reproductive function and
361 knockout mice are viable. Additionally, histological inspection of the testis and epididymis of these
362 mice reveal effective spermatogenesis, with normal spermatid progression in seminiferous
363 tubules and mature sperm in their convoluted ducts. Unsurprisingly, we also see no
364 morphological defects evident by electron microscopy of sperm from MRP9 single knockouts, as
365 these male mice are perfectly capable of siring progeny even in a MRP5 heterozygous
366 background. Any discernable impact on reproduction is only found when both MRP9 and MRP5
367 are ablated. Indeed, DKO mice show significant reproductive failures due to decreased male
368 fecundity. Defects in sperm fertilization rates and high incidences of penile prolapse and seminal
369 coagulum clogging contribute to their decrease in reproductive output as measured by litter size.
370 This is likely due to the DKO sperm's inability to effectively fertilize, as supported by the
371 drastically reduced IVF rates.
372 In addition to decreased motility trends, we show substantial changes in the composition
373 of metabolites retained in the testes as well as significant perturbations in gene expression as a
374 consequence of the loss of MRP9 and MRP5. Importantly, our integrative analysis of these
375 approaches demonstrate that energy production and mitochondrial function were the most
376 impacted pathways in the DKO testes, consistent with our localization studies. Targeted high-
377 throughput metabolomics of subcellular fractions also revealed substantial changes at the
378 subcellular level. While others have shown that triglyceride species can accumulate at the whole
379 tissue level during mitochondrial dysfunction, we show that these lipid changes are occurring at
380 the mitochondria and MAMs in the DKO testes (62, 63, 76, 77).
381 The top pathway identified by our gene expression analysis was EIF2 signaling, which we
382 validated *in vivo* as a response to mitochondria dysfunction and/or induced by alterations in heme
383 levels in maturing sperm. Indeed, heme and iron related genes were differentially expressed in
384 the testes, and quantification of heme in the caudal epididymis of DKO mice showed significantly
385 decreased levels. In a similar vein to the well-established models of unfolded protein response in
386 the erythron, we envisage a necessity for heme sharing and partitioning as mitochondria are
387 rapidly being recruited and cells are undergoing proliferation for spermatogenesis and
388 differentiation. Though this translational regulation via EIF2 signaling has been well-studied in

389 other contexts, virtually nothing is known about its role in the testes. The only published study to
390 our knowledge relates to EIF2s3y, which was shown to be essential for regulating protein
391 proliferation in spermatogenesis (78). It is yet to be determined whether or not this subunit plays
392 any direct role to our findings here, although it is also significantly upregulated in the DKO testes
393 (P = 0.022).
394 Beyond EIF2 signaling, IPA identified several additional pathways: Protein Ubiquitination
395 (essential for unfolded protein response), mTOR Signaling, Regulation of EIF4, Oxidative
396 Phosphorylation, Germ Cell-Sertoli Cell Junction Signaling (an essential component of sperm
397 differentiation), and Mitochondrial Dysfunction. It is plausible that all-*trans* retinoic acid may be a
398 regulator in all these pathways for the following reasons: 1) it is essential in male fertility as one of
399 the primary signaling molecules from Sertoli cells for progression of spermatogenesis; 2) it is
400 critical for regulating gene expression of essential oxidative phosphorylation and mitochondrial
401 genes; and 3) it has been shown to modulate mTOR and EIF4 regulation (51, 52, 57). Consistent
402 with this notion, we find genes associated with retinoids and retinoic acid levels significantly
403 decreased in DKO testes. Furthermore, targets of gene expression perturbation have significant
404 enrichment of retinoic acid-related binding motifs for transcriptional regulation, albeit modulation
405 via these motifs may be indirect. RORA has been reported to act as a constitutive activator of
406 transcription in the absence of ligand and all-*trans* retinoic acid does not bind to RXR with high
407 affinity as compared to 9-*cis* retinoic acid (79, 80).
408 These systemic changes in the testes of DKO mice are in-line with the striking
409 morphological abnormality of their mitochondria at the ultrastructural level. The impact of such
410 evident dysfunction at the sperm midpiece has significant effects on male fecundity. The
411 mitochondrial sheath is essential for reproductive fitness as these tightly wrapped mitochondria
412 are critical for ATP production and maximize efficiency of energy delivery, directly correlated with
413 sperm swimming velocities across species (27, 28, 81-84). However, this immense output comes
414 with a price - because spermatozoa are so densely packed with mitochondria, they are also
415 epicenters for the production of detrimental free radicals/reactive oxygen species (27, 81, 83, 85).
416 If not balanced and mitigated, this can cause myriads of problems including lipid peroxidation,
417 which has been shown to damage the sperm and decrease their mitochondrial membrane
418 potential (27, 81, 83, 86). Loss of MRP5 and MRP9 alters mitochondrial homeostasis not only
419 inducing vacuolated and aberrant mitochondria, but also resulting in a significant reduction in
420 sperm mitochondrial membrane potential as observed by JC-1 staining. This relationship between
421 mitochondrial membrane potential and sperm function directly correlates with mitochondrial
422 health, sperm motility, and modulation of respiratory chain activity and oxidative phosphorylation
423 pathways (27, 82, 87-89). Concordantly, male fecundity relies heavily on this organelle and its
424 membranes being fully intact and functional for the overall health of the spermatozoa and their
425 fertilization capacity, cementing why DKO males show such significant loss of biological function
426 (27, 81-83). Male infertility is a significant problem globally, affecting over 70 million people and
427 accounting for 50% of documented issues in infertile couples (82, 90, 91). To our knowledge,
428 mutations or SNP variants of MRPs have not yet been investigated for any correlation to cases of
429 male reproductive dysfunction. Our findings here would suggest that human patients with
430 infertility issues, typically assayed for and characterized by mitochondrial dysfunctions, may have
431 hypomorphic mutations in MRP9 and MRP5.
432
433

434 **Materials and Methods**

435 ***General methods***

436 **Animals**
437 All mice used were housed in Animal Sciences Departmental facilities at the University of
438 Maryland and kept in standard 12-hour light-dark cycles. Both sexes were used for all
439 experiments unless stipulated otherwise, such as the analysis of male sex organs and requisite

440 male reproduction phenotypes. ABCC12/MRP9 mutant mice were generated via CRISPR/Cas9
441 RNA injections at the National Human Genome Research Institute (NHGRI). Guide RNAs **(Table**
442 **S3)** were purchased from Sage Laboratories, St Louis, MO and Cas9 RNA was purchased from
443 Trilink Biotechnologies, San Diego, CA. The guide RNA and Cas9 RNA were combined at a
444 concentration of 5 ng/µl each in 10 mM Tris, 0.25 mM EDTA pH 7.5 for pronuclear injection.
445 Performed using standard procedures, fertilized eggs were collected from super-ovulated
446 C57BL/6J females approximately nine hours after mating with C57BL/6J male mice. Pronuclei
447 were injected with a capillary needle with a 1-2 µm opening pulled with a Sutter P-1000
448 micropipette puller. The RNAs were injected using a FemtoJet 4i (Eppendorf) with continuous
449 flow estimated to deposit approximately 2 pl of solution. Injected eggs were surgically transferred
450 to pseudo-pregnant CB6 F1 recipient females. DNA was then obtained from founder (F0) animals
451 by tail biopsy and sequenced to determine mutations. F0 animals carrying mutations were
452 crossed to C57BL/6 animals and the resulting heterozygous F1 animals were either intercrossed
453 to generate homozygous mutant animals or back crossed to C57BL/6 mice for propagation.
454 MRP5 mutant mice, a gift from Dr. Piet Borst (Netherlands Cancer Institute), had previously been
455 outcrossed into full C57BL/6 background and were bred to MRP9 mutant mice to generate double
456 knockouts (DKOs). MRP5 and MRP9 mice were genotyped from tail genomic DNA via PCR and
457 RFLP methods (see **Table S4** for complete primer sequences). In brief, tail snips were taken from
458 weaned 21-day old (P21) pups and digested. The MRP5 allele was determined as described
459 previously via amplification of specific MRP5 and hygromycin cassette primers (14). MRP9
460 mutants having a +17bp insertion were PCR amplified and subsequently restriction enzyme
461 digested with AvaII (specific to the mutation). All subsequent protocols described below involving
462 these animals were approved by the Institutional Animal Care and Use Committee (IACUC) at the
463 University of Maryland, College Park.

464 **Standard Immunoblotting Methods**
465 For specific detection of MRP5 and MRP9 protein lysates, as well all other general proteins
466 unless otherwise specified, the following protocol was used: Lysis in lysis buffer (0.75% NP40,
467 0.5% Triton X-100, 0.1% SDS, 1.75 mM EDTA, 1.25 mM EGTA, 0.25% DOC, 150 mM NaCl, 50
468 mM HEPES, 25 mM Tris-Cl pH 7.5) with 3x protease inhibitors (cOmplete Protease Inhibitor
469 Cocktail EDTA-free - 1 mM phenylmethylsulfonyl fluoride, 4 mM benzamidine, 2 µg/ml leupeptin,
470 and 1 µg/ml pepstatin, Roche Diagnostics, cat. number 1187358001) and 3x phosphatase
471 inhibitors (Millipore Inhibitor Cocktail Set, cat. number 524627) and sonicated twice. Protein
472 homogenates were then clarified via centrifugation at 15,000 *x g* for 15 min at 4°C and insoluble
473 pellets discarded. Total protein concentration of the supernatant was measured using the
474 Bradford assay (Bradford Reagent Protein Assay Dye Reagent, Bio-Rad, cat. number 5000006).
475 Unboiled protein samples were then mixed with 4x Laemmli sample buffer and 100 mM
476 dithiothreitol (DTT), and 100 µg of protein/lane was loaded and separated in an SDS-PAGE gel
477 and transferred to a nitrocellulose membrane. Proteins were then cross-linked to membranes by
478 UV treatment and stained with ponceau S solution for 3 minutes for protein loading control before
479 incubation in blocking buffer (5% nonfat dry milk in 0.05% PBS-Tween 20 [PBS-T]) for 1-hour
480 rocking at room temperature. Blots were then incubated overnight at 4°C in blocking buffer
481 containing primary antibody of interest; anti-MRP5 and anti-MRP9 rat monoclonal antibodies are
482 always used at a concentration of 1:200 unless specified otherwise. The following day blots are
483 rinsed once quickly (2 min) and then washed three times (15 min) in PBS-T and subsequently
484 incubated for one hour with horseradish peroxidase (HRP)-conjugated goat anti-rat IgG
485 secondary antibody at 1:20,000 (Invitrogen cat. number 31470). Blots were then rinsed again
486 once quickly, followed by three washes (20 min) with PBS-T and then developed using enhanced
487 chemiluminescence (SuperSignal West Pico PLUS Reagent, Pierce, cat. number 34580) and
488 detected using ChemiDocTM Imaging Systems (Bio-Rad). If subsequent re-probing was
489 necessary, blots were then stripped with 500 mM NaOH for 10min and rinsed quickly with DI H_2O
490 twice, and then PBS-T three times (5min) before blocking again for one hour to repeat the
491 process with subsequent antibodies.

492 **Subcellular fractionation and MAM isolation**
493 Mitochondrial Associated Membranes (MAMs) isolation and subcellular fractionizations were
494 based off of Wieckowski et al 2009 Nature Methods Protocol with minor modifications for
495 optimization of testes tissue. Age matched wildtype and double knock out male mice were
496 anesthetized with intraperitoneal injection of ketamine/xylene and then systemic perfusion was
497 performed via standard cardiac puncture method. Perfusion was performed with IB-1 buffer (225
498 mM mannitol, 75 mM sucrose, 0.5% BSA, 0.5 mM EGTA and 30 mM Tris–HCl pH 7.4) using 25
499 ml total pushed through a 30 ml syringe with a 26G needle (BD Precision Glide, cat. number
500 305111) into the left ventricle of the beating heart, which upon completion resulted in completely
501 cleared liver and kidneys. Livers and testes were then immediately harvested and placed in IB-3
502 buffer (225 mM mannitol, 75 mM sucrose and 30 mM Tris–HCl pH 7.4) on ice at 4°C and the
503 remaining isolation was performed entirely at 4°C in a cold room. A single liver or four pooled
504 testes were necessary to achieve sufficient yield of purified MAMs, which were minced and
505 combined and then lysed in IB-1 buffer via 10 strokes in a 22 gauge 5ml glass duall dounce
506 homogenizer. The homogenate was then spun down twice at 740 *x g* to remove nuclei and
507 cellular debris. The remaining supernatant was spun at 9,000 *x g* for the isolation of crude
508 mitochondria, which was subsequently washed and spun down twice at 10,000 *x g*. The first
509 10,000 *x g* spin was in IB-2 buffer (225 mM mannitol, 75 mM sucrose, 0.16% BSA and 30 mM
510 Tris–HCl pH 7.4) and then the second in IB-3 for further purification prior to a 100,000 *x g* spin
511 through a Percoll (Sigma, cat. number P1644) gradient to separate MAMs from mitochondria. The
512 original supernatant from the 9,000 *x g* spin was also spun down at 100,000 *x g* to concentrate
513 the remaining smaller organelles, plasma membranes and cytosolic proteins labeled "Membrane
514 Prep." Each of the isolated fractions "740 *x g*", "Membrane Prep", "Mitochondria" and "MAMs" as
515 well as total initial homogenate were subsequently lysed in lysis buffer and following SIM, ran
516 side by side in a Criterion Precast Gradient 4-15% SDS-PAGE gel for western blotting probing of
517 key intracellular organellar markers and proteins of interest: HSP60 (Abcam, cat. number
518 ab46798), Calnexin (Abcam, cat. number ab22595), Mitofusin 2 (Invitrogen 7H42L13, cat.
519 number 702768), MRP5 and MRP9.

520 **Histology and immunohistochemistry**
521 Paraffin-embedded tissues were sectioned at 4 μm and processed for immunohistochemistry
522 (IHC) as previously described in Pek et al with minor modifications (92). Slides were first
523 rehydrated in descending gradient from pure xylene through ethanol series (100%, 95%, 80%,
524 70%) and followed by endogenous HRP quenching before heat-induced epitope retrieval in
525 citrate buffer pH 6 (Target Retrieval Solution, DAKO, cat. number S1700). After epitope retrieval,
526 sections were then rinsed and blocked with avidin, biotin and protein blocking following Vector
527 labs ABC elite staining kit (Vector labs, cat. number PK-6104) prior to incubation with monoclonal
528 rat anti-MRP9 antibodies at 1:50 overnight at 4°C. The next day sections were then incubated
529 with secondary biotinylated anti-rat antibody for 30 minutes at room temperature. ABC tertiary
530 reagent was added and then signals were detected by DAB substrate incubation per
531 manufacturer recommendations (DAB/Metal Concentrate Peroxidase Kit. Thermo Fischer, cat.
532 number 1859346 and 1856090). Finally, slides were lightly counterstained with hematoxylin and
533 then dehydrated in opposite ascending series and mounted with DPX Mountant (Sigma, cat.
534 number 06522-100).

535 **Heme quantification**
536 To extract heme from perfused mouse tissues, a minimum of 30 mg of caudal epididymides
537 (either three or four pooled together), an entire testis or seminal vesicle were dounce
538 homogenized fresh in a minimum of five volumes of lysis solution containing 50 mM Tris/HCl pH
539 8.0, 5 mM $CaCl_2$, 50 mM NaCl, 1% Triton X-100 and 0.5% Proteinase K. Proteinase K was added
540 fresh to the buffer and the homogenate was incubated overnight at 37°C with moderate shaking.
541 The next day the Proteinase K digest is sonicated for 1 min (10 W, pulse 0.5 sec), centrifuged at
542 11,000 *x g* for 45 minutes and then the supernatant was collected for heme quantification. 20 μl
543 of the tissue lysate sample is mixed with 180 μl of 2 M oxalic acid and sample tubes are then

544 heated in a water bath set at 100°C for 30 minutes while a duplicate set of samples remain at
545 room temperature as blank controls. Fluorescence of porphyrins were then read using
546 Ex400/10nm, Em645/40nm on a BioTek microplate reader (BioTek, Synergy HT) and heme
547 content calculated based off of a heme standard curve and subtraction of blank values (parallel
548 unheated samples in oxalic acid) from samples.

549 **EIF2α phosphorylation quantification**
550 Eight age matched wildtype and double knock out male mice were sacrificed by cervical
551 dislocation, and whole testes were dissected out and rinsed in ice cold PBS. A single testis was
552 then homogenized in 500 µl standard lysis buffer with 5x protease inhibitors and 3x phosphatase
553 inhibitors, via 8 strokes in a 20 gauge 2 ml glass duall dounce homogenizer, transferred to 1.5 ml
554 Eppendorf tube and placed on ice for 15 minutes, vortexing for 15 seconds every 5 minutes.
555 Afterward, the homogenate is then sonicated for 10 seconds, twice, prior to proceeding with
556 standard clarifying spin for standard immunoblotting. For all samples, 150 µg of protein was then
557 separated on Criterion Precast Gradient 4-15% SDS-PAGE gels (Bio-Rad, cat. number 5671083)
558 and probed for phosphorylated EIF2α protein levels with rabbit anti-Eif2a S51 phosphorylation
559 polyclonal antibody (1:500 dilution) (Cell Signaling Technologies, cat. number D9G8) and Total
560 EIF2α protein levels with rabbit anti-EIF2a polyclonal antibody (1:10,000 dilution) (Cell Signaling
561 Technologies, cat. number D7D3). Additional blots were probed with rat anti-MRP5 NC3
562 monoclonal antibody (1:200) and rat anti-MRP9 M9I-27 monoclonal antibody (1:200).
563 Quantification of EIF2α S51 phosphorylation was performed by Image Lab 6.1 software (BioRad)
564 and normalized to total EIF2α protein.
565

566 ***Mouse reproduction studies***

567 **Breeding schema for general fecundity and fertility**
568 All breeding studies were performed in harem setups with one stud male mouse and two female
569 mice per cage. These harems were monitored over a period of at least 6 months to track
570 breeding of ABCC5/ABCC12 double knockout mice (-/-, -/-) as well as the requisite control
571 intercrosses of heterozygous-homozygous (+/-, -/-) and homozygous-heterozygous (-/-, +/-) mice.
572 Once successful pregnancies were determined, females were separated from males and
573 individually housed for monitoring fecundity. New female mice were then rotated in the male mice
574 cages to maintain setups of two female mice per stud male. Males unable to produce any
575 pregnancies after two months were removed and replaced. Pregnant dams were monitored at
576 least twice daily for birth of pups and overall health, litter size was recorded at birth and any
577 subsequent mortality logged through weaning was reported. Fecundity was calculated based off
578 the number of breeding setups required to achieve same number of pregnancies as well as the
579 number of offspring per litter and average productivity of litters per harem breeding setup. All
580 genetic segregation and statistics for MRP5 and MRP9 alleles were calculated on weaned P21
581 mice.

582 ***In vitro* fertilization (IVF) and general sperm characterization**
583 All IVF was conducted in HTF media (EmbryoMax, Sigma, cat. number MR-070), supplemented
584 with 3 mg/ml of BSA. Males were mated with females and assessment of mating was determined
585 by the presence of a vaginal plug. Males that were listed as plug positive were allowed to rest a
586 total of three days prior to IVF. Spermatozoa was collected from individual males and placed in
587 90 µl of TYH media supplemented with beta-methyl-cyclodextrin to induce capacitation (93).
588 Sperm samples were allowed to capacitate for a total of 45-60 minutes. A 10 µl sample was
589 diluted in 1400 µl of IVF media and assessed on an IVOS system (Hamilton Thorne CASA -
590 Computer Assisted Sperm Analyzer). Total sperm concentration, percent progressive motility and
591 percent rapid motile cells was calculated. Visual assessment of morphology was also assessed,
592 and IVF was conducted and standardized to an insemination dose of 1.0×10^6 sperm/ml for each
593 male processed. Oocytes and sperm were incubated for a total of 5 hours. Presumptive zygotes

594 were rinsed through HTF media to remove accessory sperm and cultured overnight in KSOM
595 media plus amino acids (94). The next morning, total number of two cell embryos were
596 determined and a fertilization rate calculated based on the number of two cell embryos per total
597 number of oocytes inseminated.

598 **Sperm "swim-out" collection**

599 Age matched male mice were sacrificed by cervical dislocation, and entire reproductive tracts
600 were dissected out intact to isolate the caudal epididymis. Caudal epididymides (CE) were
601 trimmed away from fat pads and the testes, rinsed once quickly (dipping) in DPBS and then
602 dabbed dried (single touch) on a kimwipe before being placed in a 35 mm dish with mineral oil.
603 Prewarmed DPBS with added 100 mg/L $MgCl_2$ and $CaCl_2$ (swim-out solution) to 37°C was then
604 added to the mineral oil in close proximity to the CEs for sperm swim-out. Swim-out was achieved
605 by snipping the CEs with dissecting micro-scissors and dragging the exposed globule with a 22G
606 needle from the mineral oil into the swim-out solution. The entire petri dish was then covered and
607 then placed in the 37°C incubator for 30min to allow for purified sperm to fully swim-out into the
608 solution. Then sperm were collected with a 1ml pipettor and spun down gently in a 1.5 ml
609 Eppendorf tube at 333 *x g* for 3 minutes, followed by resuspension in fresh swim-out buffer and
610 rocked gently for 2 minutes. This rinsing was repeated the same way again twice, and after the
611 third rinse and spin down the sperm are ready for downstream analysis.

612 **Sperm transmission electron microscopy (TEM) imaging**

613 Swim-out collected sperm were resuspended in a final 2% PFA and 1% Glutaraldehyde solution
614 for fixation, and then rinsed in 2 changes of 0.1 M Sodium Cacodylate buffer with 2.4% sucrose
615 and 8 mM $CaCl_2$. Samples were then postfixed in 2% Osmium Tetroxide in 0.1 M Sodium
616 Cacodylate buffer with 2.4% sucrose and 8 mM $CaCl_2$. Samples were rinsed thoroughly with
617 distilled water, and then en bloc stained in saturated aqueous Uranyl Acetate. Samples were then
618 dehydrated through a graded ethanol series (50%,70%, 95%, 95%, 100%, 100%, 100%, 100%).
619 Samples were transitioned into absolute Acetone for 3 changes. Then infiltrated in a 1:1 (plastic:
620 acetone) and then 3:1 (plastic: acetone) dilutions of Embed 812 and followed with 3 changes of
621 100% plastic prior to embedding. Samples were cure 24 hours in a 60°C oven. Once removed
622 from the oven samples were thick sectioned with glass knives to determine best area to thin
623 section, on a Leica EM UC6 Ultramicrotome. A diamond knife (Diatome) was used to thin section
624 samples and sections were placed on 150 hex copper grids. Grids were stained sequentially with
625 Aqueous Saturated Uranyl Acetate followed by Reynold's Lead Citrate. Sections were examined
626 at 120 KV on a JEOL 1400 plus Transmission Electron Microscope at 6000x magnification and
627 digital images were taken on a GATAN Orius camera. Representative cross-sectional planes of
628 the sperm midpieces were taken for an n > 15 FOVs for each animal sample.

629 **Sperm JC1 staining and flow cytometry**

630 JC-1, a fluorescent, cationic, lipophilic dye, was used to demonstrate differences in mitochondrial
631 membrane potential (MitoProbeTM JC-1 Assay Kit for Flow Cytometry, Invitrogen cat. number
632 M34152). In brief, sperm collected fresh from swim-out were resuspended in 500 μM swim-out
633 solution with final concentration of 3 μM JC-1 dye and gently rocked at 37°C for 20 minutes in the
634 dark prior to two rounds of rinses (333 *x g* for 3 minutes). Per manufacturer instructions, CCCP
635 (carbonyl cyanide m-chlorophenyl hydrazine) 25 μM final concentration was used as positive
636 control to disrupt mitochondrial potential and to confirm that the JC-1 response was indeed
637 sensitive. JC-1 exhibits potential-dependent accumulation of red fluorescent J-aggregates in
638 mitochondria, indicated by a fluorescence emission shift from green (~529 nm) to red (~590 nm).
639 In this way, mitochondrial depolarization can be inferred by a decrease in the red/green
640 fluorescence intensity ratio, so sperm were analyzed using a BD Biosciences FACSCanto II and
641 gated for green (FITC) and red (PE) fluorescence from a 488 laser. Percentage of sperm with
642 defective mitochondrial membrane potential FITC-pos PE-neg were gated from a minimum of

643 200,000 events per replicate. Representative sperm from each gating strategy were also sorted
644 directly onto microscope slides using BD Biosciences FACSAria II and imaged.
645

646 ***Mammalian cell culture methods***
647 All mammalian cells were cultured continuously at 37°C in a humidified incubator with 5% CO_2.
648 Immortalized fibroblasts were generated from mouse embryos isolated at E12.5 by sacrificing
649 pregnant females and culturing the mouse embryonic fibroblasts (MEFs) as described previously
650 (14, 95). Once established, these primary cells from wildtype, MRP9 single knockout and double
651 knockout mice were immortalized by retroviral infection of MEFs with conditioned media from Ψ2-
652 U195 cells producing the SV40 large T antigen. For overexpression in cell culture, plasmids for
653 either *ABCC5* or *ABCC12* constructs were transfected into cell lines using PolyJet transfection
654 reagent (SignaGen Laboratories, cat. number SL100688). Previously, human *ABCC5* ORF was
655 cloned into pcDNA3.1(+)zeo and pEGFP-N1 plasmids for mammalian expression (14). Likewise,
656 human *ABCC12* ORF was cloned into pcDNA3.1(+)zeo via EcorI and XbaI in a similar manner
657 and subsequently epitope tagged with FLAG. Cells that were transfected with either vector or
658 MRP expressing constructs could then be harvested up to 48 hours later for western blotting
659 (protein expression), microscopy (localization) or other downstream assays. For attempting
660 induction of endogenous expression of MRP5 or MRP9 in cell lines possibly capable of
661 production (i.e. T-47D, A549, HCT116 and GC-2spd), cells were treated for 24 hours with 2 mM
662 Sodium Butyrate (NaB) following methods from Bin Shi et al 2020 and then analyzed for
663 expression and subcellular localization (72). For western blotting, cells were harvested in
664 standard lysis buffer and followed standard immunoblotting procedure as described above. For
665 polarization of MDCKII cells, trypsinized cells were seeded onto transwell cell culture inserts
666 (Corning, COSTAR Polystyrene 6 well plates 24mm inserts, cat. number 3450) and allowed to
667 grow to a monolayer in standard growth media (DMEM supplemented with 10% FBS) changed
668 daily. Prior to reaching confluence, MDCKII cell's monolayer integrity was determined daily by
669 measuring the transepithelial electrical resistance (TEER) using an $EVOM^2$ Epithelial
670 Voltohmmeter device (World Precision Instruments, cat. number EVOM2). MDCKII cells were
671 considered polarized and used for imaging when TEER values exceeded 200 Ω/cm^2 resistance
672 and were validated by checking for markers of polarization. Immunofluorescence was performed
673 as follows: cells seeded onto coverslips (or transwells) were rinsed with ice cold DPBS (and
674 subsequently in between each additional step) and immediately fixed in freshly prepared 4% PFA
675 for greater than 30 minutes; cells were then quenched with 0.1 M ethanolamine for 5 minutes,
676 twice; permeabilized with 0.1% Triton-X 100 in DPBS solution for 10 minutes; and blocked in
677 blocking solution of 3% BSA:Superblock (SuperBlock Buffer in PBS, Thermo Scientific, cat.
678 number 37515) for greater than one hour at room temperature or overnight at 4°C; incubated with
679 primary antibody (rat monoclonal anti-MRP9 M9I-38, 1:10 in blocking solution) overnight at 4°C;
680 secondary antibody (Alexa fluorophore-conjugated goat anti-rat, 1:2000 in blocking solution) for 1
681 hour at RT; and subsequently counterstained with DAPI (1:30,000 of 5 mg/ml) for 3 minutes and
682 mounted using Antifade reagent (ProLong Gold Antifade Reagent, Invitrogen, cat. number
683 P36934). Images were taken and processed using an Airyscan980 SR confocal microscope
684 (Zeiss).
685

686 ***Metabolomics methods***

687 **Global untargeted metabolomics of mouse testes**
688 Tissue was first extracted either in aqueous or organic methods. For aqueous extractions, 10
689 volumes of methanol:H_2O (3:1) was added to the tissue sample and homogenized with ceramic
690 beads (Precellys®24-Dual, PeqLab). Then 200 µl of the homogenate was transferred to a new
691 tube where it was then vortexed and centrifuged at 15,000 RPM for 10 min at 4°C. The
692 supernatant was transferred to sample vial for ultra high performance liquid chromatography
693 coupled with mass spectrometry (UHPLC-MS) analysis. Analytes were separated with either a

694 CSH C18 column or a BEH amide column for more nonpolar and polar species, respectively. For
695 the first aqueous method, separation was achieved using an ACQUITY UPLC CSH C18 Column
696 (1.7 µm, 2.1 mm X 100 mm). Mobile phase A was water (contained 0.1% formic acid) and mobile
697 phase B was acetonitrile (contained 0.1% formic acid). The gradient was: 0 to 1 min, 5% B; 1.1 to
698 10 min, 5% to 95 % B; 10.1 to 13 min, 95 % B; 13.1 to 13.5 min, 95 to 5% B; 13.6 to 15 min, hold
699 at 5% B. The flow rate was 0.5 mL/min. The column was maintained at 50°C and the auto-
700 sampler was kept at 10°C. A 5 µL injection was used for all samples. For the second method of
701 aqueous analysis, the separation was achieved using an ACQUITY UPLC BEH amide Column
702 (1.7 µm, 2.1 mm X 100 mm). Mobile phase A was water (contained 0.1% formic acid) and mobile
703 phase B was acetonitrile (contained 0.1% formic acid). The gradient was: 0 to 1 min, 99% B; 1 to
704 10 min, 99% to 30 B; 10.1 to 12 min, hold at 99% B. The flow rate was 0.5 mL/min. The column
705 was maintained at 45°C and the auto-sampler was kept at 10°C. A 5 µL injection was used for all
706 samples. For both aqueous sample preps, data was acquired in both positive (HDMSe) and
707 negative (HDMSe) mode. The capillary voltages were separated for positive (0.8 kV) and
708 negative (0.8 kV) and sampling cone voltage was 40 V. Nitrogen at a flow of 800 L/h was used as
709 the desolvation gas with a constant desolvation temperature of 500°C. The source temperature
710 was set at 150°C. Data were acquired over the *m/z* range of 50-1000. For organic extraction
711 (lipid) methods, likewise 10 volumes of methanol:H_2O (3:1) was added to the tissue sample and
712 homogenized with ceramic beads (Precellys®24-Dual, PeqLab). However, now after
713 homogenization 400 ul was transferred to a new tube and 500 µL of ice-cold methyl-tert-butyl
714 ether (MTBE) is added, prior to incubation at 650 RPM for 1 hour. Additionally, 500 µL of ice-cold
715 water was then added and incubated at 650 RPM for 15 min before phase separation was
716 completed by centrifugation for 8 min at 8,000 RPM at 4°C. The top (organic) layer was removed
717 and dried at room temperature under nitrogen. The recovered lipids were reconstituted in 200 µL
718 of isopropanol:acetonitrile:water (2:1:1, v/v/v) and were transferred to sample vial for UPLC-MS
719 analysis. The separation was achieved using a CORTECS HILIC Column (2.7 µm, 2.1 mm X 100
720 mm). Mobile phase A was water/acetonitrile (5:95, v/v) with 10 mM ammonium acetate and
721 mobile phase B water/acetonitrile (50:50, v/v) with 10 mM ammonium acetate. The gradient was
722 ramped from 0.1% to 20% B in 10 min, ramped to 80% B in 3 min, ramped back down to 0.1% B
723 and held for 3 min. The flow rate was 0.5 mL/min. The column was maintained at 30°C and the
724 auto-sampler was kept at 10°C. A 5 µL injection was used for all samples. Like the aqueous
725 phase, data was acquired in both positive (HDMSe) and negative (HDMSe) mode. The capillary
726 voltages were separated for positive (2.8 kV) and negative (1.9 kV) and sampling cone voltage
727 was 30 V. Nitrogen at a flow of 900 L/h was used as the desolvation gas with a constant
728 desolvation temperature of 550°C. The source temperature was set at 120°C. Data were
729 acquired over the *m/z* range of 100-1500. Positive and negative mode data were basally
730 analyzed by Progenesis QI and putative metabolite identification was searched by using HMDB
731 and LIPID MAPS databases (delta < 5 ppm). The output marker lists were then manually sorted
732 and annotated for more sophisticated downstream analysis with MetaboAnalyst (96-98).
733 Multivariate data analysis, volcano plots, Variable Importance in Projection (VIP) heat maps and
734 mummichog algorithm analysis to putatively annotate metabolites were performed using
735 MetaboAnalyst 4.0 (35).

736 **Measurement of retinoids from reproductive tissues**

737 Two separate analyses were performed to determine the retinoid profile in wild type and double
738 knockout mice. Testes and seminal vesicles were assayed for retinoic acid isomers and retinol
739 and total retinyl esters. Tissue samples were stored in -80°C until processed. Only glass
740 containers, pipettes, and syringes were used to handle retinoids. Extraction of retinoids was
741 performed under yellow lights using a two-step liquid-liquid extraction that has been described in
742 detail previously using 4,4-dimethyl-RA as an internal standard for RA and retinyl acetate as an
743 internal standard for retinol and total retinyl ester (99-102). Briefly, for the extraction of retinoids,
744 tissue was homogenized in 1 mL of 0.9% NaCl (normal saline) and to each homogenate aliquot,
745 3 mL of 0.025 M KOH in ethanol was added to the homogenate followed by addition of 10 mL
746 hexane to the aqueous ethanol phase. The samples were vortexed and centrifuged for 1 to 3 min

747 at 1,000 rpm in a Dynac centrifuge (Becton Dickinson) to facilitate phase separation and pellet
748 precipitated protein. The hexane (top) phase containing nonpolar retinoids [retinol and total retinyl
749 esters (RE)] was removed. Then 4 M HCl (200 µL) was added to the remaining aqueous ethanol
750 phase, samples were vortexed, and then polar retinoids (RA) were removed by extraction with a
751 second 10 mL aliquot of hexane as described above. Organic hexane phases were evaporated
752 under nitrogen while heating at approximately 30°C in a water bath (model N-EVAP 112,
753 Organomation Associates, Berlin, MA, USA). All samples were resuspended in 60 µL acetonitrile.
754 Levels of RA were determined by liquid chromatography-multistage tandem mass spectrometry
755 (LC-MRM^3) which is an LC-MS/MS method utilizing two distinct fragmentation events for
756 enhanced selectivity (99). RA was measured using a Shimadzu Prominence UFLC XR liquid
757 chromatography system (Shimadzu, Columbia, MD) coupled to an AB Sciex 6500+ QTRAP
758 hybrid triple quadrupole mass spectrometer (AB Sciex, Framingham, MA) using atmospheric
759 pressure chemical ionization (APCI) operated in positive ion mode as previously described (99).
760 For the LC separation, the column temperature was controlled at 25°C, the autosampler was
761 maintained at 10°C and the injection volume was typically 20 µL. All separations were performed
762 using an Ascentis Express RP-Amide guard cartridge column (Supelco, 50 × 2.1 mm, 2.7 µm)
763 coupled to an Ascentis Express RP-Amide analytical column (Supelco, 100 × 2.1 mm, 2.7 µm).
764 Mobile phase A consisted of 0.1% formic acid in water, and mobile phase B consisted of 0.1%
765 formic acid in acetonitrile. Endogenously occurring retinoid isomers including all-trans-retinoic
766 acid (RA), 9-*cis* retinoic acid, 13-*cis* retinoic acid, and 9,13-di-*cis* retinoic acid are resolved using
767 a gradient separation at a flow rate of 0.4 mL min^{-1} with gradient conditions described previously
768 (99). The APCI source conditions and MRM^3 detection parameters were as previously described
769 where the MRM^3 transition for RA was *m/z* 301.1 → *m/z* 205.1 → *m/z* 159.1 and for 4,4-
770 dimethyl RA was *m/z* 329.2 → *m/z* 151.2 → *m/z* 100.0 (99).
771 Levels of retinol and total retinyl esters (RE) were quantified via HPLC-UV according to previously
772 published methodology (102, 103). Note: total retinyl esters is 90+% retinyl palmitate. Retinol and
773 RE were resolved by reverse-phase chromatography (Zorbax SB-C18, 4.6 × 100 mm, 3.5 µm) on
774 a Waters Acquity UPLC H-class system and were quantified by UV absorbance at 325 nm.
775 Analytes were separated at 1 mL min^{-1} with a gradient separation as described previously with a
776 typical injection volume of 30 µL. The amount of retinoic acid (RA), retinol (ROL) and total retinyl
777 ester (RE) was normalized per gram of tissue.

778 **Targeted metabolomics of subcellular fractionation of testes**
779 High-Throughput Targeted Metabolomics were performed on subcellular fractions isolated from
780 WT and DKO testes. This subcellular fractionation was performed as described above with minor
781 modifications, generating "Total Homogenate", "740 *x g*", "Membrane Prep", "Mitochondria" and
782 "MAMs" fractions. In order to maintain compatibility with downstream mass spectrometry analysis,
783 each fraction was collected in ice cold 0.9% saline for its final centrifugation and subsequently
784 was rinsed and diluted in ice cold 0.9% saline instead of lysis buffer prior to freezing. The
785 concentration of metabolites and lipids were then determined with mass spectrometry using
786 MxP® Quant 500 kit (Biocrates Life Sciences AG, Innsbruck, Austria). The kit enables
787 quantification of approximately 630 endogenous metabolites belonging to 26 different biochemical
788 classes: alkaloids (1), amine oxides (1), amino acids (20), amino acids related compounds (30),
789 bile acids (14), biogenic amines (9), carbohydrates (1), carboxylic acids (7), cresols (1), fatty
790 acids (12), hormones (4), indoles and derivatives (4), nucleobases and related compounds (2),
791 vitamins (1), acylcarnitines (40), lysophosphatidylcholines (14), phosphatidylcholines (76),
792 sphingomyelins (15), ceramides (28), dihydroceramides (8), hexosylceramides (19),
793 dihexosylceramides (9), trihexosylceramides (6), cholesteryl esters (22), diglycerides (44),
794 triglycerides (242). The method combines direct infusion coupled with tandem mass spectrometry
795 (DI – MS/MS) and reverse phase liquid chromatography coupled with tandem mass spectrometry
796 workflows (LC – MS/MS). Extraction was carried out per manufacturer's instructions. Tissue
797 samples were homogenized with ceramic beads (Precellys®24-Dual, Bertin Technologies SAS,
798 France) prior to analysis. Briefly, mitochondrial fractions and tissue homogenates were thawed
799 over ice and 30 µl of the sample was loaded onto the filter plate in 96 well format, impregnated

800 with deuterated internal standards and dried under a stream of nitrogen in a positive pressure
801 manifold. A 5% solution of phenylisothiocyanate in ethanol:water:pyridine (1:1:1, v:v:v) was added
802 for derivatization of metabolites. Extraction was done with 5 mM ammonium acetate in methanol.
803 The extracts were eluted with positive pressure manifold, followed by dilution steps for LC-MS/MS
804 and DI-MS/MS acquisitions. The tandem mass spectrometry platform consisted of a Waters I
805 Class Ultra performance liquid chromatography (UPLC) coupled to a Waters TQ-XS tandem
806 quadrupole mass spectrometer (Waters Corporation, Milford, MA). MetIDQ software (Biocrates
807 Life Sciences AG, Innsbruck, Austria) was used to register the samples, analyze the data and
808 validate the assay. All reagents used were of analytical grade and mobile phases used were of
809 LC-MS grade.

810 ***Transcriptomics and associated methods***

811 **RNAseq of mouse testes**
812 RNA was extracted from frozen tissues following standard Trizol chloroform protocol (Invitrogen,
813 cat. number 15596026) and aqueous fractions were then taken directly into Qiagen RNA plus
814 extraction kit (Qiagen, cat. number 74136) for maximum purity. Total RNA quality and quantity
815 were tested on an Agilent Bioanalyzer 2100 System (Agilent cat. number G2939BA) using RNA
816 Nano Chip On-Chip Electrophoresis trays for samples with RIN scores greater than 8 prior to
817 processing for library prep/construction and sequencing. RNA-seq was performed at NISC using
818 Illumina NovaSeq6000. FastQC, version 0.11.7, was used as an additional bioinformatics quality
819 control on output reads from sequencing. The reads were then aligned to the mouse mm10
820 GRCh38 reference genome for gene annotation using STAR (Spliced Transcripts Alignment to a
821 Reference), version 2.7.0f, and numbers of reads in transcripts per million (TPM) mapped to
822 genes were counted generating matrixes for all samples. Differentially expressed genes were
823 then identified via both manual export, sorting and fold change annotation, as well as processed
824 via DESeq2, version 1.12.3, for more complex analysis. DESeq2 was run using R (version 3.6.1)
825 and Bioconductor (version 3.4) with BioInstaller (version 1.24.0) for volcano plotting and statistical
826 analysis of differential changes utilizing adjusted *P* value < 0.01 and False Discovery Rate (FDR)
827 cutoffs of 0.05. The complete RNA sequencing results have been depositing to the NCBI Gene
828 Expression Omnibus under accession under GSE176740.

829 **Pathway analysis**
830 Gene Ontology (GO) enrichment and network analysis of RNAseq results were performed using
831 both Ingenuity Pathway Analysis (IPA) software package (Qiagen version 1-16) and manually
832 developed excel pipeline workflows. For IPA analysis, statistically significant gene lists by tissue
833 were manually filtered for minimum threshold of 10 TPM, sorted by *P* value and uploaded along
834 with gene expression fold change for analysis. For pipeline pathway analysis, gene lists for GO
835 terms and associated pathways of interest were downloaded from MGI (104-106), RGD (107) as
836 well as manually added from literature review of relevant publications. These all-encompassing
837 lists were then used as target gene IDs for filtered call look up functions from RNAseq gene
838 expression RSEM matrixes. In brief, genes with matching IDs which passed threshold of
839 expression in at least one sample condition and were statistically significant, were output in a
840 heatmap with *P* value and relative fold change displayed.

841 **Motif analysis**
842 The MEME Suite and HOMER motif platforms were used to unbiasedly identify conserved motifs
843 via discovery analysis of enriched sequences from differentially expressed genes. More
844 specifically, we generated gene lists (either globally or mitochondria targeted) and divided them
845 into upregulated and downregulated genes and extracted their associated sequence FASTA files.
846 Then 1000bp upstream of ORF and 50bp downstream were used to run MEME or HOMER via
847 Perl scripts on NIH High Performance Cluster (HPC) to discover the top 5 ungapped enriched
848 putative motif sequences. These sequences were then further analyzed with the web-based suite

849 tools TomTom and GoMo for MEME motif findings and manually curated for motif verification,
850 which were further validated by checking and annotating output from the HOMER suite.

851 ***Additional Bioinformatics and statistical analyses***
852 All alignment and evolutionary analyses were conducted using MEGA X software version 10.2.4
853 (108-111). All data throughout are expressed as means ± SEM unless otherwise stated. Means of
854 groups were assessed by using two-sided, unpaired student's t-test or the equivalent analyses
855 where applicable unless otherwise stated. A P value of < 0.05 when compared to baseline values
856 or genotypes (WT) was considered statistically significant. All analyses were performed using
857 Prism 9 software (GraphPad, version 9.1.0).
858

859 **Acknowledgments**
860
861 We would like to acknowledge Ms. Lisa Garrett for conducting the pronuclear injections at
862 NHGRI, NIH to generate the *ABCC12* mouse. We also thank Mr. Simon Beardsley for sharing the
863 *C. elegans mrp-5* data. We acknowledge the Imaging Core Facility in the Department of Cell
864 Biology and Molecular Genetics at the University of Maryland, College Park supported by Award
865 Number 1S10OD025223-01A1 from the National Institutes of Health. This work was also done in
866 part by utilizing the computational resources of the National Institutes of Health HPC Biowulf
867 cluster (http://hpc.nih.gov). The MRP5 (M5I-10, M5-NC3) and MRP9 (M9I-27, M9I-38, M9II-3)
868 antibodies used throughout were a generous gift from Piet Borst / Koen van de Wetering
869 (Netherlands Cancer Institute). This work was supported by funding from the National Institutes of
870 Health DK85035 and DK125740 (IH); HD077260 (MAK); the Utah Center for Iron and Heme
871 Disorders was supported by funding from DK110858 (JP); and the Intramural Program of the
872 National Human Genome Research Institute (DB). The funders had no role in study design, data
873 collection and analysis, decision to publish, or preparation of the manuscript.
874
875

876 **References**

877 1. M. Kool *et al.*, Analysis of expression of cMOAT (MRP2), MRP3, MRP4, and MRP5,
878 homologues of the multidrug resistance-associated protein gene (MRP1), in human
879 cancer cell lines. *Cancer Res* **57**, 3537-3547 (1997).
880 2. M. A. McAleer, M. A. Breen, N. L. White, N. Matthews, pABC11 (Also Known as MOAT-C
881 and MRP5), a Member of the ABC Family of Proteins, Has Anion Transporter Activity but
882 Does Not Confer Multidrug Resistance When Overexpressed in Human Embryonic
883 Kidney 293 Cells. *Journal of Biological Chemistry* **274**, 23541-23548 (1999).
884 3. P. Borst, R. Evers, M. Kool, J. Wijnholds, A family of drug transporters: the multidrug
885 resistance-associated proteins. *J Natl Cancer Inst* **92**, 1295-1302 (2000).
886 4. G. D. Kruh, M. G. Belinsky, The MRP family of drug efflux pumps. *Oncogene* **22**, 7537-
887 7552 (2003).
888 5. P. M. Jones, A. M. George, The ABC transporter structure and mechanism: perspectives
889 on recent research. *Cellular and Molecular Life Sciences CMLS* **61**, 682-699 (2004).
890 6. A. J. Slot, S. V. Molinski, S. P. Cole, Mammalian multidrug-resistance proteins (MRPs).
891 *Essays Biochem* **50**, 179-207 (2011).
892 7. J.-Y. Lee, D. M. Rosenbaum, Transporters Revealed. *Cell* **168**, 951-953 (2017).
893 8. B. Sarkadi, M. Müller, Z. Holló, The multidrug transporters—proteins of an ancient
894 immune system. *Immunology Letters* **54**, 215-219 (1996).
895 9. I. B. Holland, M. A. Blight, ABC-ATPases, adaptable energy generators fuelling
896 transmembrane movement of a variety of molecules in organisms from bacteria to
897 humans. *Journal of Molecular Biology* **293**, 381-399 (1999).
898 10. S. Cole *et al.*, Overexpression of a transporter gene in a multidrug-resistant human lung
899 cancer cell line. *Science* **258**, 1650-1654 (1992).
900 11. S. P. C. Cole, Targeting Multidrug Resistance Protein 1 (MRP1, ABCC1): Past, Present,
901 and Future. *Annual Review of Pharmacology and Toxicology* **54**, 95-117 (2014).
902 12. C. A. Ritter *et al.*, Cellular export of drugs and signaling molecules by the ATP-binding
903 cassette transporters MRP4 (ABCC4) and MRP5 (ABCC5). *Drug Metab Rev* **37**, 253-278
904 (2005).
905 13. R. G. Deeley, C. Westlake, S. P. Cole, Transmembrane transport of endo- and xenobiotics
906 by mammalian ATP-binding cassette multidrug resistance proteins. *Physiol Rev* **86**, 849-
907 899 (2006).
908 14. T. Korolnek, J. Zhang, S. Beardsley, G. L. Scheffer, I. Hamza, Control of metazoan heme
909 homeostasis by a conserved multidrug resistance protein. *Cell Metab* **19**, 1008-1019
910 (2014).
911 15. G. Jedlitschky, B. Burchell, D. Keppler, The multidrug resistance protein 5 functions as an
912 ATP-dependent export pump for cyclic nucleotides. *J Biol Chem* **275**, 30069-30074
913 (2000).
914 16. G. Reid *et al.*, Characterization of the Transport of Nucleoside Analog Drugs by the
915 Human Multidrug Resistance Proteins MRP4 and MRP5. *Molecular Pharmacology* **63**,
916 1094-1103 (2003).
917 17. R. S. Jansen, S. Mahakena, M. de Haas, P. Borst, K. van de Wetering, ATP-binding
918 Cassette Subfamily C Member 5 (ABCC5) Functions as an Efflux Transporter of
919 Glutamate Conjugates and Analogs. *J Biol Chem* **290**, 30429-30440 (2015).
920 18. X. Yuan *et al.*, Regulation of intracellular heme trafficking revealed by subcellular
921 reporters. *Proc Natl Acad Sci U S A* **113**, E5144-5152 (2016).

922 19. R. K. Donegan, C. M. Moore, D. A. Hanna, A. R. Reddi, Handling heme: The mechanisms
923 underlying the movement of heme within and between cells. *Free Radical Biology and*
924 *Medicine* **133**, 88-100 (2019).
925 20. I. G. Chambers, M. M. Willoughby, I. Hamza, A. R. Reddi, One ring to bring them all and
926 in the darkness bind them: The trafficking of heme without deliverers. *Biochim Biophys*
927 *Acta Mol Cell Res* **1868**, 118881 (2021).
928 21. A. R. Reddi, I. Hamza, Heme Mobilization in Animals: A Metallolipid's Journey. *Accounts*
929 *of Chemical Research* **49**, 1104-1110 (2016).
930 22. J. Tammur *et al.*, Two new genes from the human ATP-binding cassette transporter
931 superfamily, ABCC11 and ABCC12, tandemly duplicated on chromosome 16q12. *Gene*
932 **273**, 89-96 (2001).
933 23. T. K. Bera *et al.*, MRP9, an unusual truncated member of the ABC transporter
934 superfamily, is highly expressed in breast cancer. *Proc Natl Acad Sci U S A* **99**, 6997-7002
935 (2002).
936 24. N. Ono *et al.*, Multidrug resistance-associated protein 9 (ABCC12) is present in mouse
937 and boar sperm. *Biochem J* **406**, 31-40 (2007).
938 25. H. Shimizu *et al.*, Characterization of the mouse Abcc12 gene and its transcript encoding
939 an ATP-binding cassette transporter, an orthologue of human ABCC12. *Gene* **310**, 17-28
940 (2003).
941 26. M. Jung *et al.*, Unified single-cell analysis of testis gene regulation and pathology in five
942 mouse strains. *Elife* **8** (2019).
943 27. A. Amaral, B. Lourenço, M. Marques, J. Ramalho-Santos, Mitochondria functionality and
944 sperm quality. *REPRODUCTION* **146**, R163-R174 (2013).
945 28. N.-H. Gu, W.-L. Zhao, G.-S. Wang, F. Sun, Comparative analysis of mammalian sperm
946 ultrastructure reveals relationships between sperm morphology, mitochondrial
947 functions and motility. *Reproductive Biology and Endocrinology* **17**, 66 (2019).
948 29. D. Stojanovski, M. Bohnert, N. Pfanner, M. van der Laan, Mechanisms of Protein Sorting
949 in Mitochondria. *Cold Spring Harb Perspect Biol* **4** (2012).
950 30. J. Lee, D. H. Kim, I. Hwang, Specific targeting of proteins to outer envelope membranes
951 of endosymbiotic organelles, chloroplasts, and mitochondria. *Frontiers in Plant Science* **5**
952 (2014).
953 31. J. E. Vance, MAM (mitochondria-associated membranes) in mammalian cells: lipids and
954 beyond. *Biochim Biophys Acta* **1841**, 595-609 (2014).
955 32. M. R. Wieckowski, C. Giorgi, M. Lebiedzinska, J. Duszynski, P. Pinton, Isolation of
956 mitochondria-associated membranes and mitochondria from animal tissues and cells.
957 *Nature Protocols* **4**, 1582-1590 (2009).
958 33. P. Pinton, Mitochondria-associated membranes (MAMs) and pathologies. *Cell Death Dis*
959 **9**, 413 (2018).
960 34. M. Yang *et al.*, Mitochondria-Associated ER Membranes – The Origin Site of Autophagy.
961 *Frontiers in Cell and Developmental Biology* **8** (2020).
962 35. S. Li *et al.*, Predicting Network Activity from High Throughput Metabolomics. *PLOS*
963 *Computational Biology* **9**, e1003123 (2013).
964 36. D. Phillips, A. M. Aponte, S. A. French, D. J. Chess, R. S. Balaban, Succinyl-CoA synthetase
965 is a phosphate target for the activation of mitochondrial metabolism. *Biochemistry* **48**,
966 7140-7149 (2009).

967 37. I. Martínez-Reyes, N. S. Chandel, Mitochondrial TCA cycle metabolites control
968 physiology and disease. *Nature Communications* **11**, 102 (2020).
969 38. J. J. Chen, S. Zhang, Heme-regulated eIF2alpha kinase in erythropoiesis and
970 hemoglobinopathies. *Blood* **134**, 1697-1707 (2019).
971 39. A. P. Han *et al.*, Heme-regulated eIF2alpha kinase (HRI) is required for translational
972 regulation and survival of erythroid precursors in iron deficiency. *EMBO J* **20**, 6909-6918
973 (2001).
974 40. J. Igarashi *et al.*, Elucidation of the Heme Binding Site of Heme-regulated Eukaryotic
975 Initiation Factor 2α Kinase and the Role of the Regulatory Motif in Heme Sensing by
976 Spectroscopic and Catalytic Studies of Mutant Proteins. *Journal of Biological Chemistry*
977 **283**, 18782-18791 (2008).
978 41. R. N. V. S. Suragani *et al.*, Heme-regulated eIF2α kinase activated Atf4 signaling pathway
979 in oxidative stress and erythropoiesis. *Blood* **119**, 5276-5284 (2012).
980 42. H. Mellor, K. M. Flowers, S. R. Kimball, L. S. Jefferson, Cloning and characterization of
981 cDNA encoding rat hemin-sensitive initiation factor-2 alpha (eIF-2 alpha) kinase.
982 Evidence for multitissue expression. *Journal of Biological Chemistry* **269**, 10201-10204
983 (1994).
984 43. J. J. Berlanga, S. Herrero, C. de Haro, Characterization of the Hemin-sensitive Eukaryotic
985 Initiation Factor 2α Kinase from Mouse Nonerythroid Cells*. *Journal of Biological*
986 *Chemistry* **273**, 32340-32346 (1998).
987 44. A. B. Page *et al.*, Persistent eIF2alpha(P) is colocalized with cytoplasmic cytochrome c in
988 vulnerable hippocampal neurons after 4 hours of reperfusion following 10-minute
989 complete brain ischemia. *Acta Neuropathol* **106**, 8-16 (2003).
990 45. T. Tsuyama, A. Tsubouchi, T. Usui, H. Imamura, T. Uemura, Mitochondrial dysfunction
991 induces dendritic loss via eIF2α phosphorylation. *Journal of Cell Biology* **216**, 815-834
992 (2017).
993 46. S. Zhang *et al.*, HRI coordinates translation necessary for protein homeostasis and
994 mitochondrial function in erythropoiesis. *eLife* **8**, e46976 (2019).
995 47. Y. Miyagi *et al.*, Abundant expression of translation initiation factor EIF-4E in post-
996 meiotic germ cells of the rat testis. *Laboratory investigation; a journal of technical*
997 *methods and pathology* **73**, 890-898 (1995).
998 48. J. Marill, N. Idres, C. C. Capron, E. Nguyen, G. G. Chabot, Retinoic acid metabolism and
999 mechanism of action: a review. *Curr Drug Metab* **4**, 1-10 (2003).
1000 49. N. Y. Kedishvili, Enzymology of retinoic acid biosynthesis and degradation: Thematic
1001 Review Series: Fat-Soluble Vitamins: Vitamin A. *Journal of Lipid Research* **54**, 1744-1760
1002 (2013).
1003 50. T. J. Cunningham, G. Duester, Mechanisms of retinoic acid signalling and its roles in
1004 organ and limb development. *Nature Reviews Molecular Cell Biology* **16**, 110-123 (2015).
1005 51. H. B. Everts, C. D. Berdanier, Regulation of Mitochondrial Gene Expression by Retinoids.
1006 *IUBMB Life (International Union of Biochemistry and Molecular Biology: Life)* **54**, 45-49
1007 (2002).
1008 52. R. Puttagunta, S. Di Giovanni, Retinoic acid signaling in axonal regeneration. *Front Mol*
1009 *Neurosci* **4**, 59 (2011).
1010 53. C. D. Berdanier, H. B. Everts, C. Hermoyian, C. E. Mathews, Role of vitamin A in
1011 mitochondrial gene expression. *Diabetes Res Clin Pract* **54 Suppl 2**, S11-27 (2001).

1012 54. N. NOY, Retinoid-binding proteins: mediators of retinoid action. *Biochemical Journal*
1013 **348**, 481-495 (2000).
1014 55. J. L. Napoli, Cellular retinoid binding-proteins, CRBP, CRABP, FABP5: Effects on retinoid
1015 metabolism, function and related diseases. *Pharmacology & therapeutics* **173**, 19-33
1016 (2017).
1017 56. R.-Z. Liu *et al.*, CRABP1 is associated with a poor prognosis in breast cancer: adding to
1018 the complexity of breast cancer cell response to retinoic acid. *Molecular Cancer* **14**, 129
1019 (2015).
1020 57. C. A. Hogarth, M. D. Griswold, The key role of vitamin A in spermatogenesis. *J Clin Invest*
1021 **120**, 956-962 (2010).
1022 58. J. K. Amory *et al.*, Isotretinoin administration improves sperm production in men with
1023 infertility from oligoasthenozoospermia: a pilot study. *Andrology* **5**, 1115-1123 (2017).
1024 59. J. T. Busada *et al.*, Retinoic acid regulates Kit translation during spermatogonial
1025 differentiation in the mouse. **397**, 140-149 (2015).
1026 60. M. D. Griswold, Spermatogenesis: The Commitment to Meiosis. *Physiol Rev* **96**, 1-17
1027 (2016).
1028 61. C. Peluso-Iltis, J. Osz, N. Rochel, "DNA recognition by retinoic acid nuclear receptors".
1029 (Elsevier, 2020), 10.1016/bs.mie.2020.03.001, pp. 235-260.
1030 62. S. Vankoningsloo *et al.*, Mitochondrial dysfunction induces triglyceride accumulation in
1031 3T3-L1 cells: role of fatty acid beta-oxidation and glucose. *J Lipid Res* **46**, 1133-1149
1032 (2005).
1033 63. Y. Kawano, D. E. Cohen, Mechanisms of hepatic triglyceride accumulation in non-
1034 alcoholic fatty liver disease. *Journal of Gastroenterology* **48**, 434-441 (2013).
1035 64. Y. Toyoda *et al.*, MRP class of human ATP binding cassette (ABC) transporters: historical
1036 background and new research directions. *Xenobiotica* **38**, 833-862 (2008).
1037 65. Y. K. Zhang, Y. J. Wang, P. Gupta, Z. S. Chen, Multidrug Resistance Proteins (MRPs) and
1038 Cancer Therapy. *AAPS J* **17**, 802-812 (2015).
1039 66. A. Lorico *et al.*, Disruption of the murine MRP (multidrug resistance protein) gene leads
1040 to increased sensitivity to etoposide (VP-16) and increased levels of glutathione. *Cancer*
1041 *Res* **57**, 5238-5242 (1997).
1042 67. J. Wijnholds *et al.*, Increased sensitivity to anticancer drugs and decreased inflammatory
1043 response in mice lacking the multidrug resistance-associated protein. *Nature medicine*
1044 **3**, 1275-1279 (1997).
1045 68. C. J. F. De Wolf *et al.*, cGMP transport by vesicles from human and mouse erythrocytes.
1046 *FEBS Journal* **274**, 439-450 (2007).
1047 69. G. Jedlitschky, B. Burchell, D. Keppler, The Multidrug Resistance Protein 5 Functions as
1048 an ATP-dependent Export Pump for Cyclic Nucleotides. *Journal of Biological Chemistry*
1049 **275**, 30069-30074 (2000).
1050 70. P. Borst, C. de Wolf, K. van de Wetering, Multidrug resistance-associated proteins 3, 4,
1051 and 5. *Pflugers Arch* **453**, 661-673 (2007).
1052 71. D. M. Klein, S. H. Wright, N. J. Cherrington, Localization of Multidrug Resistance-
1053 Associated Proteins along the Blood-Testis Barrier in Rat, Macaque, and Human Testis.
1054 *Drug Metabolism and Disposition* **42**, 89-93 (2014).
1055 72. B. Shi *et al.*, Effect of sodium butyrate on ABC transporters in lung cancer A549 and
1056 colorectal cancer HCT116 cells. *Oncol Lett* **20**, 148-148 (2020).

1057 73. S. Costello *et al.*, Ca2+-stores in sperm: their identities and functions. *Reproduction*
1058 *(Cambridge, England)* **138**, 425-437 (2009).
1059 74. K. K. Karna, Y. S. Shin, B. R. Choi, H. K. Kim, J. K. Park, The Role of Endoplasmic Reticulum
1060 Stress Response in Male Reproductive Physiology and Pathology: A Review. *The World*
1061 *Journal of Men's Health* **37** (2019).
1062 75. X. Ying *et al.*, Endoplasmic reticulum protein 29 (ERp29), a protein related to sperm
1063 maturation is involved in sperm-oocyte fusion in mouse. *Reprod Biol Endocrinol* **8**, 10-10
1064 (2010).
1065 76. T. Klopstock *et al.*, Mitochondrial DNA mutations in multiple symmetric lipomatosis.
1066 *Molecular and Cellular Biochemistry* **174**, 271-275 (1997).
1067 77. A. Muñoz-Málaga *et al.*, Lipomatosis, proximal myopathy, and the mitochondrial 8344
1068 mutation. A lipid storage myopathy? *Muscle & Nerve* **23**, 538-542 (2000).
1069 78. S. Mazeyrat *et al.*, A Y-encoded subunit of the translation initiation factor Eif2 is
1070 essential for mouse spermatogenesis. *Nature Genetics* **29**, 49-53 (2001).
1071 79. J. M. Harris, P. Lau, S. L. Chen, G. E. Muscat, Characterization of the retinoid orphan-
1072 related receptor-alpha coactivator binding interface: a structural basis for ligand-
1073 independent transcription. *Mol Endocrinol* **16**, 998-1012 (2002).
1074 80. G. Allenby *et al.*, Retinoic acid receptors and retinoid X receptors: interactions with
1075 endogenous retinoic acids. *Proc Natl Acad Sci U S A* **90**, 30-34 (1993).
1076 81. N. Srivastava, M. Pande, Mitochondrion: Features, functions and comparative analysis of
1077 specific probes in detecting sperm cell damages. *Asian Pacific Journal of Reproduction* **5**,
1078 445-452 (2016).
1079 82. K. Nowicka-Bauer *et al.*, Sperm mitochondrial dysfunction and oxidative stress as
1080 possible reasons for isolated asthenozoospermia. *J Physiol Pharmacol* **69** (2018).
1081 83. J. D. D. A. Losano *et al.*, Spermatic mitochondria: role in oxidative homeostasis, sperm
1082 function and possible tools for their assessment. *Zygote* **26**, 251-260 (2018).
1083 84. G. E. Olson, V. P. Winfrey, Structural organization of surface domains of sperm
1084 mitochondria. *Molecular Reproduction and Development* **33**, 89-98 (1992).
1085 85. M. Maneesh, H. Jayalekshmi, Role of reactive oxygen species and antioxidants on
1086 pathophysiology of male reproduction. *Indian J Clin Biochem* **21**, 80-89 (2006).
1087 86. Adam J. Koppers, Lisa A. Mitchell, P. Wang, M. Lin, R. J. Aitken, Phosphoinositide 3-
1088 kinase signalling pathway involvement in a truncated apoptotic cascade associated with
1089 motility loss and oxidative DNA damage in human spermatozoa. *Biochemical Journal*
1090 **436**, 687-698 (2011).
1091 87. A. Amaral, J. Ramalho-Santos, Assessment of mitochondrial potential: implications for
1092 the correct monitoring of human sperm function. *Int J Androl* **33**, e180-186 (2010).
1093 88. A. Amaral *et al.*, Identification of proteins involved in human sperm motility using high-
1094 throughput differential proteomics. *J Proteome Res* **13**, 5670-5684 (2014).
1095 89. A. Alamo *et al.*, Mitochondrial Membrane Potential Predicts 4-Hour Sperm Motility.
1096 *Biomedicines* **8**, 196 (2020).
1097 90. K. Hwang, R. C. Walters, L. I. Lipshultz, Contemporary concepts in the evaluation and
1098 management of male infertility. *Nat Rev Urol* **8**, 86-94 (2011).
1099 91. J. Fainberg, J. A. Kashanian, Recent advances in understanding and managing male
1100 infertility. *F1000Res* **8** (2019).
1101 92. R. H. Pek *et al.*, Hemozoin produced by mammals confers heme tolerance. *eLife* **8**
1102 (2019).

1103 93. N. Nakagata, "Cryopreservation of Mouse Spermatozoa and In Vitro Fertilization" in
1104 Transgenic Mouse Methods and Protocols, M. H. Hofker, J. van Deursen, Eds. (Humana
1105 Press, Totowa, NJ, 2011), 10.1007/978-1-60761-974-1_4, pp. 57-73.
1106 94. Y. Ho, K. Wigglesworth, J. J. Eppig, R. M. Schultz, Preimplantation development of mouse
1107 embryos in KSOM: Augmentation by amino acids and analysis of gene expression.
1108 *Molecular Reproduction and Development* **41**, 232-238 (1995).
1109 95. D. A. Williams, M. F. Rosenblatt, D. R. Beier, R. D. Cone, Generation of murine stromal
1110 cell lines supporting hematopoietic stem cell proliferation by use of recombinant
1111 retrovirus vectors encoding simian virus 40 large T antigen. *Molecular and Cellular*
1112 *Biology* **8**, 3864-3871 (1988).
1113 96. J. Chong *et al.*, MetaboAnalyst 4.0: towards more transparent and integrative
1114 metabolomics analysis. *Nucleic Acids Res* **46**, W486-W494 (2018).
1115 97. J. Chong, M. Yamamoto, J. Xia, MetaboAnalystR 2.0: From Raw Spectra to Biological
1116 Insights. *Metabolites* **9**, 57 (2019).
1117 98. J. Chong, D. S. Wishart, J. Xia, Using MetaboAnalyst 4.0 for Comprehensive and
1118 Integrative Metabolomics Data Analysis. *Current Protocols in Bioinformatics* **68**, e86
1119 (2019).
1120 99. J. W. Jones, K. Pierzchalski, J. Yu, M. A. Kane, Use of fast HPLC multiple reaction
1121 monitoring cubed for endogenous retinoic acid quantification in complex matrices. *Anal*
1122 *Chem* **87**, 3222-3230 (2015).
1123 100. M. A. Kane, N. Chen, S. Sparks, J. L. Napoli, Quantification of endogenous retinoic acid in
1124 limited biological samples by LC/MS/MS. *Biochem J* **388**, 363-369 (2005).
1125 101. M. A. Kane, A. E. Folias, C. Wang, J. L. Napoli, Quantitative profiling of endogenous
1126 retinoic acid in vivo and in vitro by tandem mass spectrometry. *Anal Chem* **80**, 1702-
1127 1708 (2008).
1128 102. M. A. Kane, J. L. Napoli, Quantification of endogenous retinoids. *Methods Mol Biol* **652**,
1129 1-54 (2010).
1130 103. M. A. Kane, A. E. Folias, J. L. Napoli, HPLC/UV quantitation of retinal, retinol, and retinyl
1131 esters in serum and tissues. *Anal Biochem* **378**, 71-79 (2008).
1132 104. C. J. Bult, J. A. Blake, C. L. Smith, J. A. Kadin, J. E. Richardson, Mouse Genome Database
1133 (MGD) 2019. *Nucleic Acids Res* **47**, D801-d806 (2019).
1134 105. T. F. Hayamizu, M. Mangan, J. P. Corradi, J. A. Kadin, M. Ringwald, The Adult Mouse
1135 Anatomical Dictionary: a tool for annotating and integrating data. *Genome Biol* **6**, R29
1136 (2005).
1137 106. C. L. Smith, J. T. Eppig, The mammalian phenotype ontology: enabling robust annotation
1138 and comparative analysis. *Wiley Interdiscip Rev Syst Biol Med* **1**, 390-399 (2009).
1139 107. J. R. Smith *et al.*, The Year of the Rat: The Rat Genome Database at 20: a multi-species
1140 knowledgebase and analysis platform. *Nucleic Acids Res* **48**, D731-d742 (2020).
1141 108. N. Saitou, M. Nei, The neighbor-joining method: a new method for reconstructing
1142 phylogenetic trees. *Mol Biol Evol* **4**, 406-425 (1987).
1143 109. E. Zuckerkandl, L. Pauling, "Evolutionary Divergence and Convergence in Proteins" in
1144 Evolving Genes and Proteins, V. Bryson, H. J. Vogel, Eds. (Academic Press, 1965),
1145 https://doi.org/10.1016/B978-1-4832-2734-4.50017-6, pp. 97-166.
1146 110. S. Kumar, G. Stecher, M. Li, C. Knyaz, K. Tamura, MEGA X: Molecular Evolutionary
1147 Genetics Analysis across Computing Platforms. *Mol Biol Evol* **35**, 1547-1549 (2018).

1148 111. G. Stecher, K. Tamura, S. Kumar, Molecular Evolutionary Genetics Analysis (MEGA) for
1149 macOS. *Mol Biol Evol* **37**, 1237-1239 (2020).

1150
1151

Figures and Tables

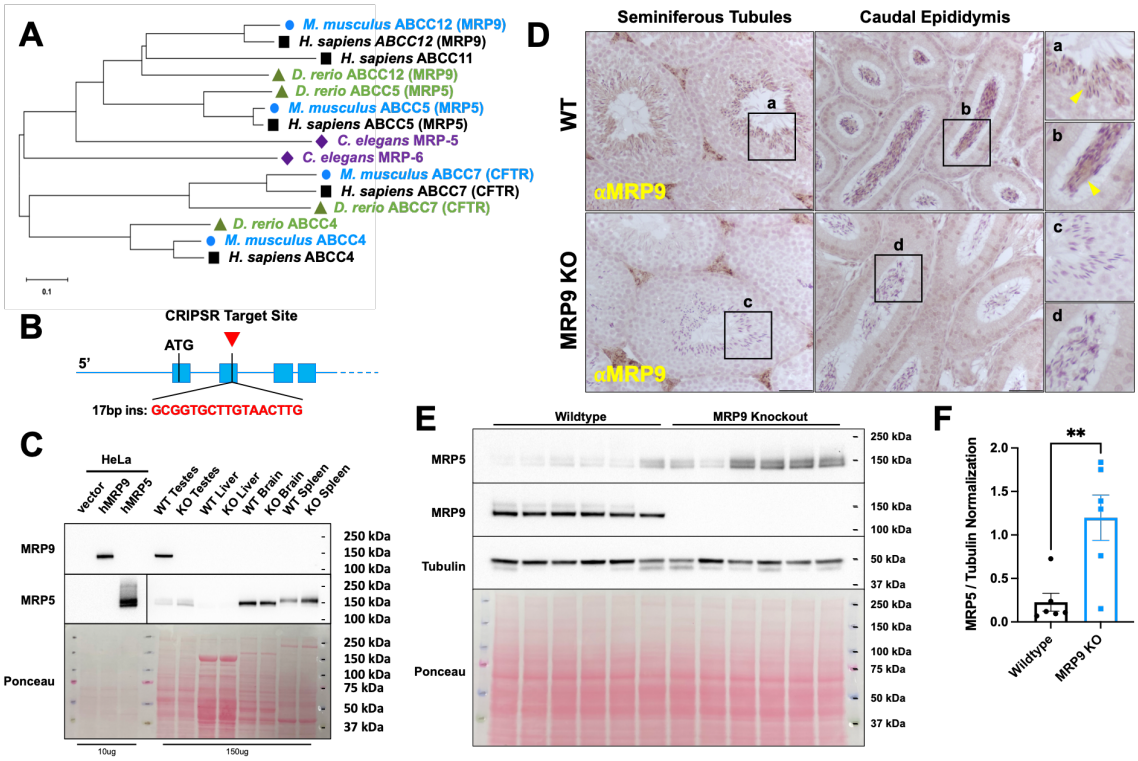

Figure 1. Ablation of MRP9 in mice induces MRP5 expression in the testes

{A} Amino acid FASTA sequences for MRPs in humans, mice, zebrafish and worms were aligned and used to generate the optimal phylogenetic tree shown. The evolutionary history was inferred using the Neighbor-Joining method. The tree is drawn to scale, with branch lengths in the same units as those of the evolutionary distances used to infer the phylogenetic tree. The evolutionary distances were computed using the Poisson correction method and are in the units of the number of amino acid substitutions per site. **{B}** Gene loci schematic of 5' UTR and the first four exons of *Abcc12* indicating the CRISPR target site in second exon for the generation of knockout MRP9 mice. **{C}** Immunoblot of protein lysates from transfected HeLa cells and Wildtype and MRP9 KO tissues probed for MRP9 and MRP5. **{D}** MRP9 immunohistochemistry analysis of paraffin-embedded testes tissue sections from WT and MRP9 KO mice. Tissue sections were probed for MRP9 and lightly counterstained with hematoxylin. Images are representative of at least 3 mice; scale bar equals 100 μm. **{E}** Immunoblot of protein lysates from wildtype and MRP9 KO testes (n=6) probed for MRP5, MRP9 and Tubulin. **{F}** Quantification of MRP5 protein expression in wildtype and MRP9 KO testes from subpanel E, normalized to Tubulin; *P* value = 0.0061.

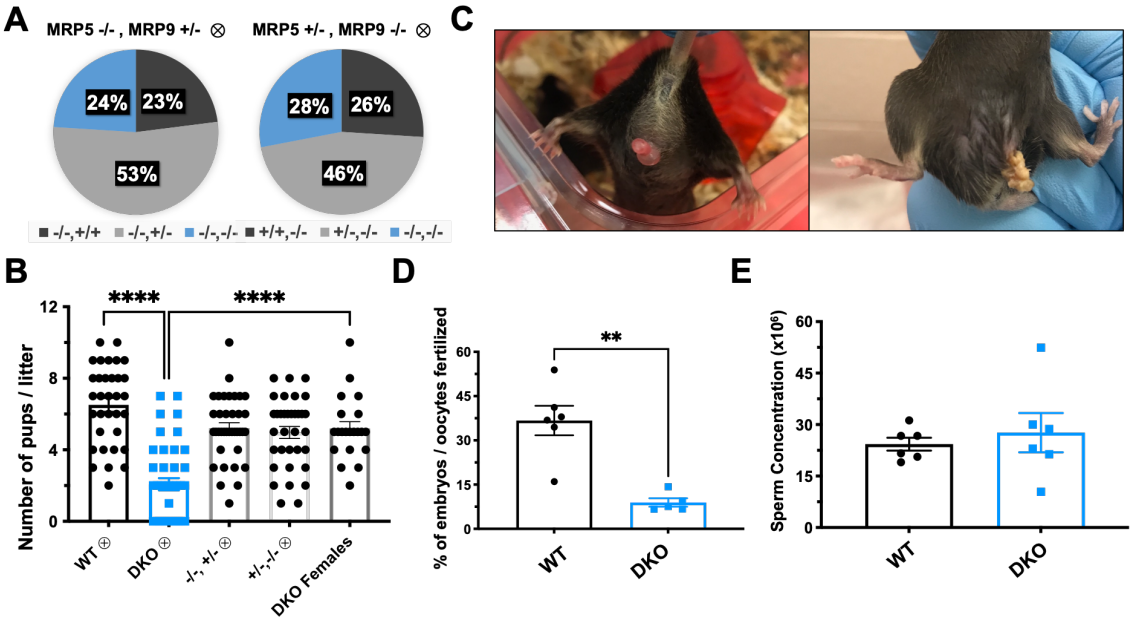

Figure 2. DKO mice are viable but have reduced male reproductive fecundity

{A} Genotyped progeny from MRP5-/- and MRR9+/- intercrosses (left), n = 190, Chi-squared = 0.568 and *P* value = 0.753; Genotyped progeny from MRP5+/- and MRR9-/- intercrosses (right), n = 166, Chi-squared = 0.976 and *P* value = 0.614. **{B}** Quantification of the number of pups weaned per litter of intercrossed WT, DKO, MRP5-/- MRR9+/-, MRP5+/- MRR9-/-, and DKO females crossed with WT or double het mice, **** *P* value < 0.0001. **{C}** Representative images of penile prolapse (left) and expressed seminal coagulum (right) in DKO male mice setup for breeding. **{D}** *In vitro* fertilization rate of WT and DKO sperm incubated with WT oocytes for 5 hours at a concentration of 1.0 x 10^6 sperm/ml. Next day total number of two cell embryos were determined and fertilization rate was calculated based on dividing by the total number of oocytes inseminated for each male, ** *P* value = 0.0019. **{E}** Total concentration of spermatozoa calculated by IVOS system computer assisted sperm analyzer.

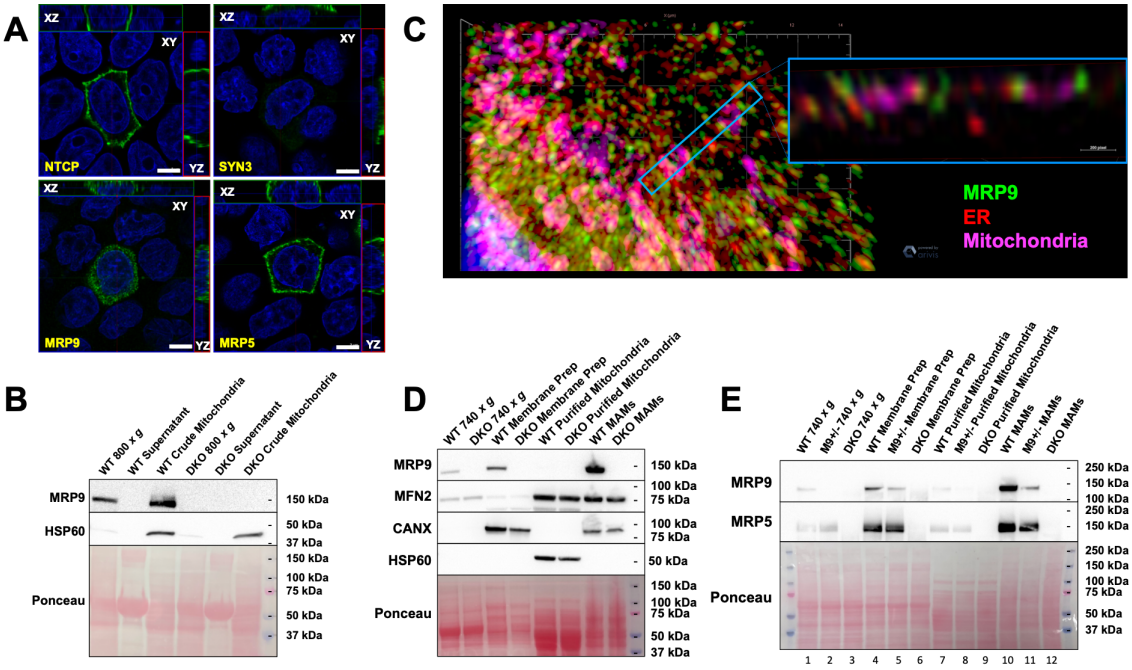

Figure 3. MRP9 is enriched in mitochondrial associated membranes (MAMs) of the testes

{A} MDCKII cells grown on transwell filters transfected with basolateral marker sodium taurocholate cotransporting polypeptide *NTCP-GFP*, apical marker syntaxin 3 *SYN3-GFP*, *ABCC12* or *ABCC5*. Polarization of the monolayers was additionally confirmed prior to fixation by measurement of trans-epithelial electrical resistance. A representative confocal section (XY) is depicted along with the composite stacks in the side panel views (XZ and YZ), scale bar equals 5 μm. **{B}** Immunoblot analysis of crude mitochondrial fractionation from testes of mice. Membrane was probed for MRP9 and HSP60, a mitochondrial matrix protein marker. **{C}** Airyscan super resolution microscopy and 3D rendering of HeLa cells transfected with human *ABCC12* for 48 hours and treated with Mitotracker Deep Red FM immediately prior to fixation and immunofluorescence. Antibody probing for MRP9 and Calnexin was followed by Alexa-488 and Alexa-568 secondary antibodies respectively followed by DAPI counter staining prior to mounting. **{D}** Immunoblot analysis of subcellular fractionation from testes of mice. Membranes were probed for MRP9 (M9II-3 antibody) and MFN2, CANX, HSP60 markers of outer mitochondrial membrane, ER membrane, and mitochondrial matrix respectively. **{E}** Immunoblot of subcellular fractionation from testes of wildtype, MRP9 heterozygous and double knockout mice. Membranes were probed for MRP9 (M9I-27 antibody) and MRP5.

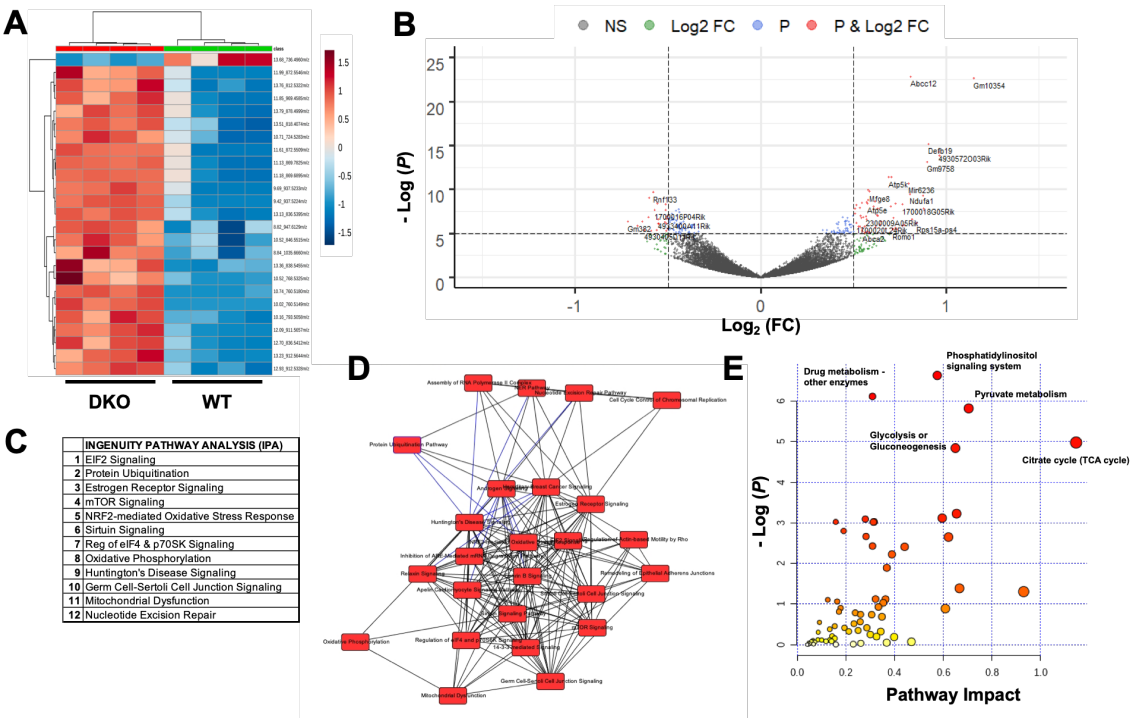

Figure 4. Metabolomics and transcriptomics reveal pervasive perturbation in DKO testes **{A}** Variable Importance in Projection (VIP) Heatmap of the top 25 differential metabolites in testes from aqueous phase extractions on C18 column run in negative mode**.** **{B}** Volcano plot of gene expression changes from DKO and WT testes; significance threshold set at -log(*P* value) > 5. **{C}** Top twelve Gene Ontology (GO) Pathways perturbed in DKO testes based on Qiagen IPA analysis. **{D}** Key overlapping canonical pathways in testes based on Qiagen IPA analysis. **{E}** MetaboAnalyst pathway impact analysis from combining RNAseq differential gene expression changes and metabolomics mummichog putative KEGG IDs of the testes; top five pathways by *P* value are annotated.

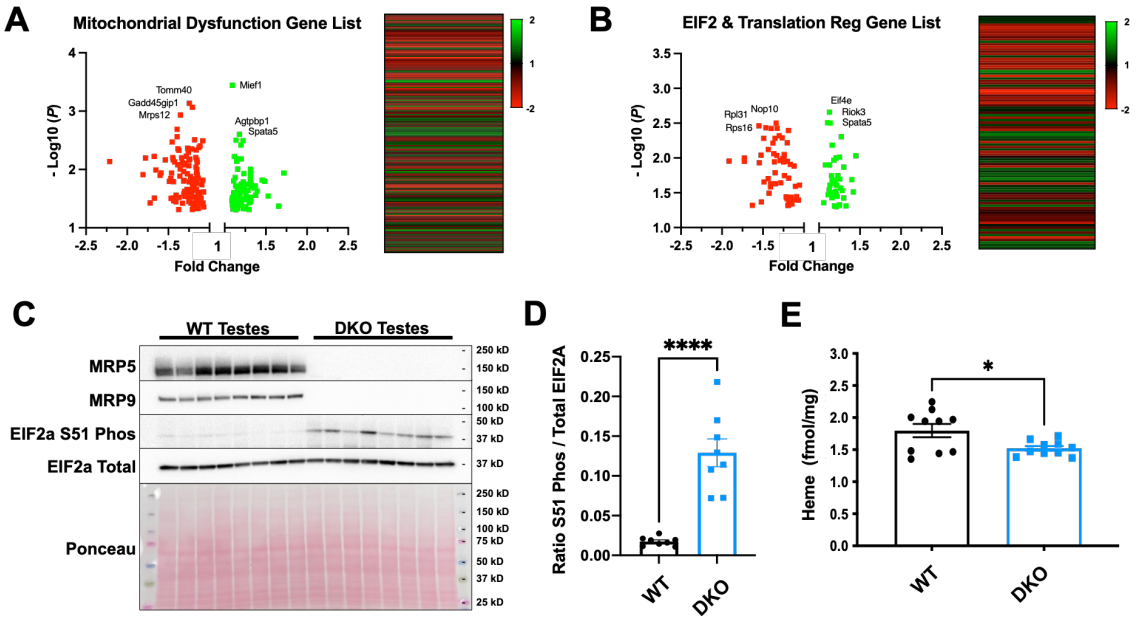

Figure 5. Loss of MRP5 and MRP9 induces EIF2 signaling to mitigate mitochondrial dysfunction

{A} Output of pathway pipeline analysis investigating all "mitochondria" and "mitochondrial disfunction" GO pathway gene lists. Gene lists were curated for integration with RNA expression data. Real expression was validated by thresholding a minimum 10 transcripts per million and statistically significant genes ($P < 0.05$) fold change were output in volcano plot and heatmap with 200 total genes identified, sorted by ascending *P* value. **{B}** Output of pathway pipeline analysis investigating all "EIF2 signaling" and "translational regulation" GO pathway gene lists. Gene lists were curated for integration with RNA expression data. Real expression was validated by thresholding a minimum 10 transcripts per million and statistically significant genes ($P < 0.05$) fold change were output in volcano plot and heatmap with 95 total genes identified, sorted by ascending *P* value. **{C}** Immunoblot analysis of testes lysates from DKO and WT mice probed for MRP5, MRP9, Serine 51 phosphorylated EIF2a and total EIF2a protein. Blot is representative of three separate experiments, each lane represents an individual mouse, n=8 mice per genotype. **{D}** Quantification of DKO and WT phosphorylated EIF2a normalized to total EIF2a protein in subpanel C, **** *P* value < 0.0001. **{E}** Heme content of pooled caudal epididymides from DKO and WT mice by oxalic acid quantification, n=15 animals per genotype (1.5 mice or 3 epididymides per replicate), * *P* value = 0.0275.

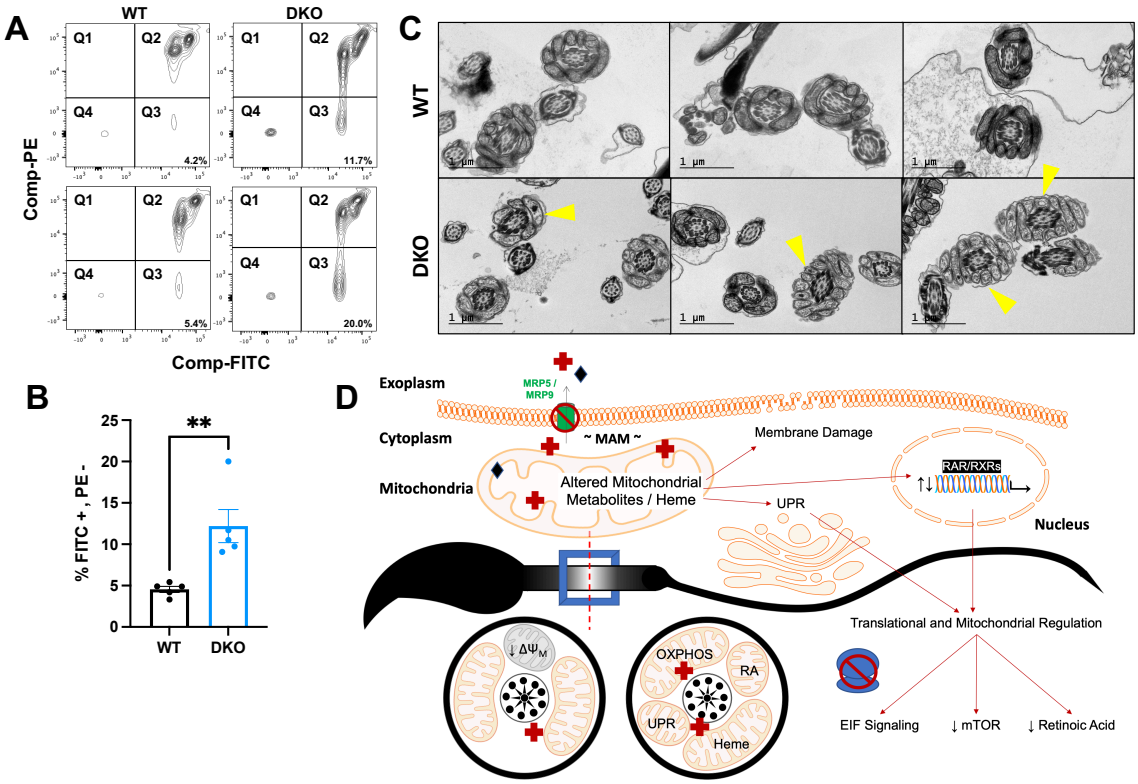

Figure 6. Spermatozoa are severely compromised by the combined loss of MRP5 and MRP9

{A} Representative sorting analysis of WT and DKO sperm stained with JC-1. Q3 is gating for populations that are FITC-pos and PE-neg representing a reduction J-aggregates / red fluorescence and therefore decreased mitochondrial membrane potential. **{B}** Quantification of sperm stained with JC-1 and gated for populations that are FITC-pos and PE-neg (from subpanel 6a), n=5 animals, ** *P* value = 0.0055. **{C}** TEM of swum-out caudal epididymal spermatozoa from WT (top) and DKO (bottom). Cross sections of the sperm midpiece visualize cristae and mitochondrial morphology of the mitochondrial sheath. Yellow arrow heads highlight vacuolated and aberrant mitochondria. Representative images from at least 15 FOVs per sample, scalebar equal 1 µm. **{D}** Model figure – the combined ablation of MRP9 and MRP5 causes inappropriate trafficking or distribution of metabolites such as heme and/or other substrates inducing mitochondrial damage. This dysfunction induces signaling through the EIF2 and mTOR pathways to regulate protein translation and UPR with corresponding changes in retinoic acid levels and signaling. Germ cells differentiate into mature spermatozoa, but these are functionally defective as they fail to fertilize normal oocytes due to mitochondrial insufficiencies.